

Liquid film distribution around long gas bubbles propagating in rectangular capillaries

M. Magnini^{1*}, F. Municchi^{1,2}, I. El Mellas¹, M. Icardi³

¹ *Department of Mechanical, Materials and Manufacturing Engineering, University of Nottingham, Nottingham NG7 2RD, United Kingdom*

² *Colorado School of Mines, 1500 Illinois St., Golden, CO 80401*

³ *School of Mathematics, University of Nottingham, Nottingham NG7 2RD, United Kingdom*

Abstract

We present a systematic analysis of the bubble and liquid film dynamics corresponding to the propagation of long, isolated gas bubbles, within rectangular capillary channels of cross-sectional aspect-ratio ranging from 1 to 8. Direct numerical simulations of the flow are performed using ESI-OpenFOAM v.1812 and its geometric Volume-Of-Fluid solver isoAdvector. The interface curvature, which enters the calculation of the surface tension force in the momentum equation, is calculated with a parabolic reconstruction method. This study covers a range of capillary and Reynolds numbers of, respectively, $0.005 \leq Ca \leq 1$ and $1 \leq Re \lesssim 1000$. The lubrication film surrounding the bubble is always resolved by the computational mesh, and thus the present results are representative of a perfectly wetting fluid. This study shows that rectangular cross-sections promote the formation of an extended liquid film covering the longer wall of the channel. This liquid film exhibits a saddle-like shape and its streamwise evolution varies depending on the channel shape and flow conditions. Although cross-sectional liquid film profiles and corresponding thicknesses are not constant along the bubble, in general the film deposited upon the shorter wall becomes thicker for increasing values of the aspect-ratio, while the thickness of the film deposited upon the longer wall obeys a $Ca^{2/3}/(1 + Ca^{2/3})$ law which, provided that the channel hydraulic radius is the same, is independent of the aspect-ratio at sufficiently small Ca . An empirical correlation is proposed to predict the cross-sectional gas fraction and bubble speed as a function of a modified capillary number, embedding dependencies on both Ca and aspect-ratio, and converging to the asymptotic limit for a quasi-static flow when $Ca \rightarrow 0$.

Keywords: Bubbles, Surface tension, Microchannel, Two-Phase, Volume-Of-Fluid, Thin film

1. Introduction

When a long gas bubble advances within a capillary tube filled with a wetting liquid, a thin film of liquid is deposited at the channel walls. The liquid film thickness and morphology depend on the shape of the channel cross-section and on the effect of viscous, capillary and inertial forces, under the assumption that the size of the channel is sufficiently small for gravitational forces to be negligible. Within circular channels, the bubble exhibits a cylindrical body with a liquid film of uniform thickness far from the front and rear menisci, and both correlations and theoretical models based on lubrication theory are available to estimate the liquid film thickness [1, 2, 3], or predict the entire bubble profile [4] as a function of the governing nondimensional groups, i.e. capillary ($Ca = \mu_l U / \sigma$, with μ_l being the liquid dynamic viscosity, σ the surface tension and U the bubble or liquid speed) and Reynolds ($Re = 2\rho_l U R_h / \mu_l$, with ρ_l being the liquid density and R_h the channel hydraulic radius) numbers.

The bubble and liquid film dynamics appear significantly different in a square channel, where a cylindrical bubble body is achieved only when $Ca > 0.04$ [5, 6, 7, 8, 9]. For smaller capillary numbers, the liquid film becomes non-axisymmetric and the transversal interface curvature gradients induce draining flows that drive liquid from the thin

*Corresponding author. E-mail: mirco.magnini@nottingham.ac.uk

film towards the channel corners. As a consequence, the liquid film thins indefinitely towards the bubble rear and a region of constant film thickness along the bubble body is never established [9]. Empirical correlations to predict the film thickness in square channels exist [3, 10], although these exhibit some discrepancy with data from direct numerical simulations [9, 8], which can be ascribed to small, but not negligible, effects of gravitational forces on the film thicknesses measured in experiments. Moran et al. [11] and Yu et al. [12] have demonstrated that very small Bond numbers, much smaller than unity, are sufficient for the film dynamics to deviate from the gravity-free case.

The situation complicates even further when rectangular channels are considered, because the liquid film distributes unevenly upon the two channel sides [13]. Wong et al. [14] applied lubrication theory to study the liquid film deposited on the walls of polygonal capillaries in the asymptotic limit $Ca \rightarrow 0$. They found that surface tension forces rearrange the liquid film into static menisci of circular shape at the channel corners, connected by thin saddle-shaped liquid films covering the channel walls. The film thicknesses obey different scaling laws depending on the distance from the bubble nose, with the centreline thickness being of order $Ca^{2/3}$ as long as $z \leq Ca^{-5/3}$ (with z being the streamwise distance from the bubble nose) and then decreasing as $Ca^{1/4}z^{-1/4}$ when $z \gg Ca^{-5/3}$. An interface dimple forms at the point of connection between the static meniscus at the channel corner and the saddle-shaped film at the centre, and the local film thickness scales as Ca^1 for $1 < z < Ca^{-1}$, while it thins to order $Ca^{4/3}$ at longer distance from the bubble nose. Hazel and Heil [8] performed numerical simulations of the propagation of air fingers within rectangular channels of aspect-ratio $1 \leq \epsilon \lesssim 2$, for Ca up to about 10. They observed that the bubble cross-section can still recover axisymmetric profiles as long as $\epsilon < 2.04$, but this happens at increasing distances from the bubble tip as Ca increases. de Lózar et al. [15] measured cross-sectional liquid area fractions and finger widths when air fingers penetrate in rectangular channels, for $1 \leq \epsilon \leq 15$ and a range of capillary numbers $10^{-4} < Ca < 3$. They observed that, for $\epsilon \geq 8$, the relative width of the air finger becomes independent of ϵ and the results approach the Hele-Shaw cell limit. In a subsequent publication [16], the same authors performed systematic numerical simulations to investigate the impact of channel aspect-ratio ($1 \leq \epsilon \leq 8$) and capillary number ($10^{-3} < Ca < 10$) on finger width and cross-sectional liquid area fraction, also including gravitational effects. For $Ca > 10^{-2}$, their results showed that the relative finger width decreases and the liquid area fraction increases with increasing the channel aspect-ratio, while there exists a modified capillary number which, incorporating a dependence on the channel aspect-ratio, is effective in collapsing all liquid fraction data onto a single curve for all aspect-ratios.

In summary, although the literature about the liquid film thickness and perimetral distribution in circular and square channel cross-sections is relatively vast, bubble propagation in rectangular capillaries has received far less attention. While systematic studies reporting liquid or gas cross-sectional fractions and bubble/finger widths for a range of aspect-ratios and capillary numbers exist [15, 16], little information is available on the detailed perimetral distribution of the liquid film on the channel cross-section, its streamwise evolution along the bubble and the corresponding liquid film thickness values. Also, the aforementioned studies for rectangular channels considered only the visco-capillary regime and the impact of inertial forces has been overlooked. There are many recent microfluidics applications that would benefit from an accurate knowledge of the liquid film distribution around the perimeter of noncircular capillaries. This represents an impactful parameter on the heat transfer performance of boiling flows in microchannels [9], and determines the efficiency of the capillary-driven detachment of colloids in unsaturated porous media [17].

This work presents a systematic study of the bubble and liquid film dynamics corresponding to the flow of isolated long bubbles in rectangular channels, covering channel cross-section aspect-ratios in the range $1 \leq \epsilon \leq 8$, capillary numbers $0.005 \leq Ca \leq 1$ and Reynolds numbers spanning from the visco-capillary ($Re = 1$) to the visco-inertial regime ($Re \approx 1000$). The two-phase flow is simulated using a Volume-Of-Fluid (VOF) method [18], as implemented in the TwoPhaseFlow library for ESI-OpenFOAM v.1812 recently released by Scheufler and Roenby [19], which is built upon OpenFOAM's geometric VOF solver isoAdvector [20, 21]. The rest of this article is organised as follows: in Section 2, the numerical model is introduced; the flow problem and numerical setup are presented in Section 3; the model validation is described in Section 4; Section 5 outlines the results of the systematic analysis and the conclusions are summarised in the final Section 6.

2. Numerical method

We consider the unsteady, laminar and isothermal flow of two immiscible, Newtonian fluids in incompressible flow, namely liquid and gas. The two-phase flow is simulated using OpenFOAM's geometric VOF solver isoAdvector [20], augmented with additional libraries to improve interface advection [21] and surface tension reconstruction as implemented in the TwoPhaseFlow library for OpenFOAM recently released by Scheufler and Roenby [19]; the TwoPhaseFlow library was compiled on ESI-OpenFOAM v.1812. According to VOF, liquid and gas are treated as a single mixture fluid, with the volume fraction c indicating the fraction of the computational cell volume occupied by a selected primary phase, $0 \leq c \leq 1$. A single set of mass and momentum equations is formulated and solved throughout the computational domain, these take the following form:

$$\nabla \cdot \mathbf{u} = 0 \quad (1)$$

$$\frac{\partial(\rho\mathbf{u})}{\partial t} + \nabla \cdot (\rho\mathbf{u}\mathbf{u}) = -\nabla p + \nabla \cdot \mu \left[(\nabla\mathbf{u}) + (\nabla\mathbf{u})^T \right] + \mathbf{F}_\sigma \quad (2)$$

where \mathbf{u} indicates the fluid velocity, t the time, p the pressure, ρ the density, μ the dynamic viscosity, and \mathbf{F}_σ the surface tension force vector. All the fluid-specific properties, ρ_g , ρ_l , μ_g , and μ_l , are considered constant in this work, whereas the local mixture fluid properties ρ and μ are calculated as an average over the two phases (here gas: $c = 1$; liquid: $c = 0$), e.g. density $\rho = c\rho_g + (1 - c)\rho_l$. The volume fraction field is evolved in time by solving the following transport equation:

$$\frac{\partial c}{\partial t} + \nabla \cdot (c\mathbf{u}) = 0 \quad (3)$$

In the geometric VOF method isoAdvector [20], Eq. (3) is solved according to a two-step procedure. First, a piecewise planar approximation of the interface is reconstructed in each cell where $0 < c < 1$. This is found as the isosurface of c that cuts the cell into two subvolumes corresponding to the cell's volume fraction value. Then, an interface advection step calculates the volume of fluid crossing each control volume face during the time-step, under the assumption that the previously reconstructed interface translates steadily across the control volume face; the sum of these fluxes represents the discretised version of the convective term of Eq. (3). Once the fluxes are calculated, the volume fraction value at the new time level is found. Details of the algorithm are provided by Roenby et al. [20]. For the interface reconstruction step, we adopt the novel plic-RDF method proposed by Scheufler and Roenby [21] and implemented in the library TwoPhaseFlow [19]. With this method, a first guess of the interface unit normal vector is found using gradients of the volume fraction, $\mathbf{n} = \nabla c / |\nabla c|$, as in the original PLIC (Piecewise Linear Interface Calculation) method [22]. Then, an iterative procedure is performed to improve this estimation, based on gradients of a reconstructed distance function (RDF) φ , $\mathbf{n} = \nabla\varphi / |\nabla\varphi|$, with φ being a signed distance function that identifies the shortest distance from a cell centre to the planar interface previously obtained. Compared to the original algebraic VOF method implemented in OpenFOAM's solver interFoam [23], Roenby et al. [20] have shown that isoAdvector yields sharper and more accurate interface representation in the presence of complex flow motion and arbitrary meshes, also enabling larger time-steps. Scheufler and Roenby [21] have demonstrated that isoAdvector with interface reconstruction based on the plic-RDF method exhibits second-order convergence with mesh refinement on both structured and unstructured grids, thus overcoming the poor convergence rates achieved by the original interface reconstructions based on isosurfaces.

The surface tension force \mathbf{F}_σ in the momentum Eq. (2) is formulated according to the Continuum Surface Force (CSF) method [24] and computed as $\mathbf{F}_\sigma = \sigma\kappa\nabla c$, with σ being the surface tension coefficient (considered constant) and κ the local interface curvature. Both OpenFOAM's built-in interFoam and isoAdvector solvers estimate κ based on gradients of the volume fraction, $\kappa = \nabla \cdot (\nabla c / |\nabla c|)$, as originally proposed by Brackbill et al. [24]. The accuracy of the calculation of κ is crucial for surface tension dominated flows, as errors yield spurious velocity fields whose magnitude is inversely proportional to the capillary number, and thus are particular detrimental when simulating capillary flows [25]. The TwoPhaseFlow library provides multiple options to calculate κ based on different geometrical approximations of the interface [19]. For the work presented in this article, we selected a parabolic fitting method which first fits a local paraboloid of equation:

$$f(x, y, z) = C_0x + C_1x^2 + C_2y + C_3y^2 + C_4xy + z \quad (4)$$

to the neighbour interface centres obtained in the reconstruction step, with the coefficients calculated based on a least-square minimisation, and then estimates the local interface curvature as:

$$\kappa = \frac{f_{xx}(1 + f_x) + f_{yy}(1 + f_y) - 2f_x f_y f_{xy}}{(1 + f_x^2 + f_y^2)^{3/2}} \quad (5)$$

where the subscripts denote the order of derivation. Further details about this method are provided by Scheufler and Roenby [19]. A comparison of the different surface tension modules available in the library TwoPhaseFlow with interFoam's and isoAdvector's built-in methods is provided in Appendix A.

OpenFOAM discretises the transport equations with a finite-volume method, on a collocated grid arrangement. The unsteady flow equations are integrated in time with a second-order Crank-Nicolson scheme with a blending coefficient of 0.9. The divergence operators are discretised using second-order TVD (Total Variation Diminishing) schemes [26], whereas Laplacian operators are discretised with central finite-differences. OpenFOAM's PIMPLE scheme, which is based on the PISO (Pressure Implicit Splitting of Operators) algorithm [27], is used for the pressure-velocity coupling, with 3 correction steps. The residuals thresholds for the iterative solution of the flow equations are set to 10^{-7} for the velocity and 10^{-8} for both volume fraction and pressure. The time-step of the simulation is variable and is calculated based on a maximum allowed Courant number of 0.1.

3. Problem definition and simulation setup

We consider an isolated, long gas bubble travelling steadily into a straight capillary of noncircular cross-section; Fig. 1 provides a schematic representation of the flow. To describe the flow, we adopt a Cartesian reference frame where z denotes the streamwise coordinate, while x and y indicate cross-stream coordinates, with x (y) parallel to the longer (shorter) side of the cross-section. The bubble travels along z at speed U_b , while liquid enters the channel with a fully developed laminar velocity profile of average speed U_l . The channel cross-section has width $2w$ and height $2h$, with $w \geq h$ and aspect-ratio defined as $\epsilon = w/h \geq 1$. Surface tension forces rearrange the liquid surrounding the bubble into thin films covering the central regions of the channel walls, with thick liquid lobes at the corners. The thickness and distribution of the liquid film depend on the channel aspect-ratio, on the competition between surface tension and viscous forces quantified by the capillary number $Ca = \mu_l U / \sigma$, and on the competition between inertial and viscous forces quantified by the Reynolds number $Re = 2\rho_l U R_h / \mu_l$, with R_h being the hydraulic radius of the channel. The velocity scale U can be either the bubble speed U_b , identifying the bubble capillary and Reynolds

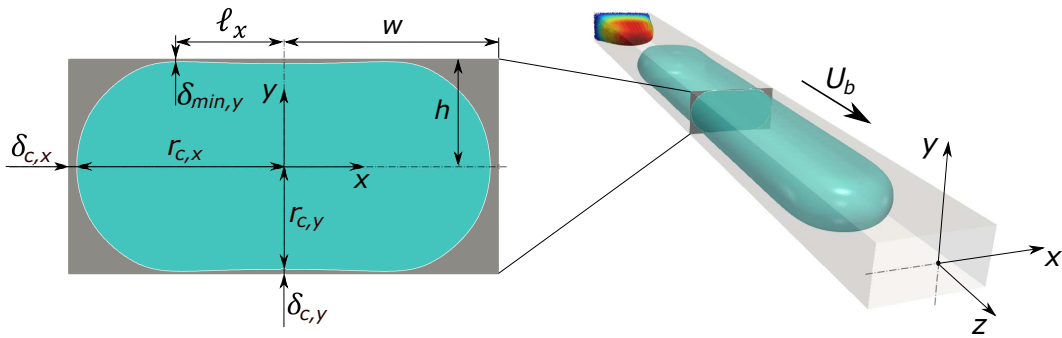


Figure 1: Schematic of the flow configuration under analysis and notation used in this work. A long gas bubble travels steadily (speed U_b) along a capillary of half-width w and half-height h , $w \geq h$; the aspect-ratio of the channel is defined as $\epsilon = w/h$, $\epsilon \geq 1$. A thin liquid film is trapped between the liquid-gas interface and the channel wall, and its thickness varies along the perimeter of the channel cross-section. We assume that the flow has $\pi/2$ symmetry on the cross-section ($x - y$ plane). The thickness of the film measured along the vertical direction at the centre of the longer wall ($x = 0$) is denoted as $\delta_{c,y}$ (vertical bubble radius: $r_{c,y} = h - \delta_{c,y}$); the thickness measured along the horizontal direction at the centre of the shorter wall ($y = 0$) is $\delta_{c,x}$ (horizontal bubble radius: $r_{c,x} = w - \delta_{c,x}$). The thin film covering the longer wall exhibits a saddle-like shape and an interfacial dimple forms at the matching point between thin film and static meniscus at the corner, where a minimum film thickness $\delta_{min,y}$ is detected at a distance ℓ_x from the wall centre.

numbers $Ca_b = \mu_l U_b / \sigma$ and $Re_b = 2\rho_l U_b R_h / \mu_l$, or the average liquid speed U_l , identifying the liquid capillary and Reynolds numbers $Ca_l = \mu_l U_l / \sigma$ and $Re_l = 2\rho_l U_l R_h / \mu_l$; note that $U_b > U_l$ owing to the presence of the lubricating film at the walls. Gravitational effects are neglected in this study. The range of channel aspect-ratios, liquid capillary and Reynolds numbers covered in this work are $\epsilon = 1-8$, $Ca_l = 0.005-0.5$ and $Re_l = 1-1000$, to which it corresponds $Ca_b = 0.0055-1$ and $Re_b = 1.1-1330$. de Lózar et al. [15] showed that the widths of air fingers propagating in rectangular capillaries for $\epsilon \geq 8$ collapse onto a single curve, thus motivating the range of ϵ selected in this study. The range of capillary and Reynolds numbers investigated is relevant to a variety of engineering applications, from the flow of high-viscosity oil through reservoir rocks [28] to that of water or low-viscosity refrigerants in microchannels for cooling applications [29].

In the numerical model, the channel is represented with a three-dimensional geometry. The hydraulic radius of the channel R_h is kept constant throughout the study; width and height vary depending on ϵ , with $2w = R_h(1 + \epsilon)$ and $2h = R_h(1 + \epsilon)/\epsilon$. At the inlet, a fully-developed laminar flow of liquid is set, together with a zero-gradient pressure condition. At the outlet, the pressure is set to a uniform reference value while a zero-gradient condition is applied to the velocity. No-slip is imposed at the channel walls. Owing to the $\pi/2$ symmetry of the flow, only one quarter of the cross-section is simulated and symmetry boundary conditions are utilised on the symmetry planes $x = 0$ and $y = 0$. A long gas bubble is initialised close to the channel inlet, as a cuboid of cross-section $1.8w \times 1.8h$ and length L_b taken as the maximum value between $5w$ and $14R_h$; this choice of L_b yields bubbles that are sufficiently long to enable comparison with the simulation results of Magnini and Matar [9] for square channels and with those of de Lózar et al. [16] for rectangular tubes. The liquid-to-gas density and viscosity ratios are set to 1000 and 100, respectively. Ca_l and Re_l are input values in our numerical model, whereas Ca_b and Re_b depend on the bubble speed resulting from the flow dynamics. At the onset, the bubble starts moving downstream and its profile evolves from that of the cuboid set at $t = 0$. As time elapses, the profile develops with the bubble nose first reaching a terminal shape, corresponding to a constant propagation speed U_b . An interfacial wave travels backward from the front to the rear of the bubble as observed by Yu et al. [30], and as the wave sweeps the bubble in the upstream direction, the bubble profile attains a steady-state shape. It is not always possible to run simulations until the entire bubble, including its rear end, has reached steady-state, because this may take very long time, in particular for $\epsilon = 8$. Therefore, simulations terminate when a sufficiently long portion of the downstream end of the bubble ($z > z_N - \max[12R_h, 4\epsilon]$, with z_N locating the tip of the nose) has achieved steady-state. All the bubble and liquid film profiles presented in the next sections verify this condition.

The domain is discretised with a structured mesh made of orthogonal hexahedra, which are gradually refined in the near-wall region in order to fully resolve the flow in the liquid film at the wall. The cross-section of the channel is discretised with 58×58 mesh elements, with 38 elements of constant size in the region $x/w, y/h = 0 - 0.9$ and 20 elements in the graded region $x/w, y/h = 0.9 - 1$, with the smallest element near the wall being of thickness $2.4 \cdot 10^{-4}w$ or $2.4 \cdot 10^{-4}h$. To avoid excessive transversal stretching of the cells, 116 cells along the channel width (x -direction) are used when $\epsilon = 8$. This mesh ensures that the liquid film at the wall is always adequately discretised in the range of conditions of interest. The same arrangement was used in previous studies by Magnini and Matar [31, 9] and tests carried out with finer meshes did not yield appreciable differences in the results. Along the flow direction, cells are twice as long as their maximum size along the y -direction. The length of the computational domain varies between $50R_h$ and $100R_h$ according to the flow conditions, with longer domains necessary to achieve steady dynamics at larger Reynolds numbers. Overall, domain grids with number of cells ranging from 3 to 10 million were utilised, with high Reynolds numbers or high aspect-ratio channels requiring more computational resources. Simulations were run on the high-performance computing cluster HPC Midlands Plus (www.hpc-midlands-plus.ac.uk), which features 28-core nodes (each with two processors Intel Xeon E5-2680v4 at 2.40 GHz, total 128 GB of memory) and Mellanox EDR infiniband interconnection. Using typically 3 computing nodes (84 cores) and OpenFOAM's scotch domain decomposition, the computational time for each simulation ranged from 5000 (low Re and aspect-ratio) to 50000 CPU hours (high Re or high aspect-ratio).

4. Validation

In order to validate the numerical model, we compare our numerical results to those obtained by de Lózar et al. [16] using the finite-element library oomph-lib (oomph-lib.maths.man.ac.uk) and a free-surface approach. **de Lózar et al. [16] simulated the propagation of an air finger at a constant speed into a tube of rectangular cross-section filled**

with a wetting liquid. Their numerical model solved the three-dimensional steady-state Stokes equations governing the flow of liquid surrounding the finger, thus disregarding inertial forces, in a reference frame moving with the finger. Non-penetration and dynamic boundary conditions were imposed at the air-liquid free-surface. In our model, we can neither neglect the convective term of the momentum equation nor set a vanishing Reynolds number value, because the time-explicit treatment of the surface tension would require an infinitely small time-step to satisfy the capillary time-step constraint [32], and thus we limit the Reynolds number to $Re = 1$. As long as the Weber number, $We = Ca Re$, is sufficiently smaller than 1, inertial effects will be negligible [4].

de Lózar et al. [16] reported measurements of the cross-sectional liquid fraction, finger width and pressure drop across the finger in the range $10^{-3} \leq Ca_b \leq 5$ and $1 \leq \epsilon \leq 8$. A comparison of the cross-sectional bubble width obtained with the present numerical framework and their numerical results is presented in Fig. 2; the right panel of the figure illustrates the liquid-gas distribution on the channel cross-section for some selected cases. The bubble width, $r_{c,x}$ (see nomenclature in Fig. 1), is measured 3.92ϵ behind the tip of the bubble nose as done by de Lózar et al. [16], and thus this distance increases with the channel aspect-ratio. As a general trend, the bubble width decreases as Ca_b is increased and viscous forces overcome surface tension. This trend changes for sufficiently high Ca_b and $\epsilon > 1$ in the data of de Lózar et al. [16]. This is attributed to the fact that the bubble width is measured at a fixed axial distance behind the tip, where the width is still dependent on the axial coordinate, while it is expected that the bubble width measured far behind the bubble tip will decrease monotonically with increasing Ca_b . For sufficiently large Ca_b , approximately $Ca_b > 0.01$, increasing the aspect-ratio yields a monotonic decrease of the relative finger width, as evident also in the cross-sectional bubble shapes illustrated in the right panels of Fig. 2. A qualitatively similar trend was observed for the width of gas fingers penetrating into liquid-filled Hele-Shaw cells by Tabeling et al. [33], who reported the linear dependency $\delta_{c,x}/w \approx 0.011/B$, with $1/B = 12\epsilon^2 Ca_b$ being the Saffman-Taylor parameter. When $Ca_b > 0.01$ and $\epsilon \geq 2$, the cross-sectional interface shape can be approximated as two semi-circles connected by two straight lines. An axial balance of pressure and viscous forces acting in the thick lateral liquid film along the dynamic meniscus at the bubble front yields [15, 16]:

$$\mu_l \left(\frac{\partial^2 u}{\partial x^2} + \frac{\partial^2 u}{\partial y^2} \right) \sim \frac{\partial p}{\partial z} \quad (6)$$

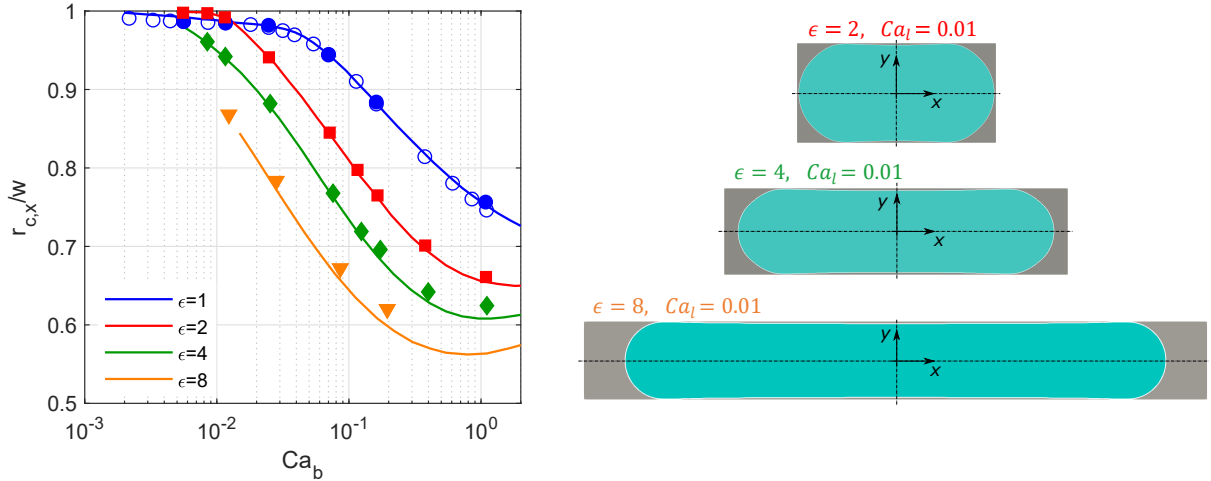


Figure 2: Horizontal bubble width $r_{c,x}$, rescaled by the channel width w , against bubble capillary number for different aspect-ratios ($We_1 \ll 1$); $r_{c,x}$ is measured 3.92ϵ behind the tip of the bubble nose. The solid lines display the numerical results of de Lózar et al. [16], which are used as a benchmark. The full symbols are the results obtained with the present numerical framework. The empty circles indicate the results obtained by Magnini and Matar [9] for a square channel, using OpenFOAM v. 2.3.1 and the built-in algebraic VOF solver interFoam. The boxes on the right display the bubble and liquid film distribution on the channel cross-section for some selected cases.

where u is the streamwise component of the fluid velocity. The viscous forces in the thick liquid lobes act along the length scales $x \sim \delta_{c,x}$ and $y \sim h$, and thus the viscous stresses can be approximated as $\mu_l \partial^2 u / \partial x^2 \sim \mu_l U_b / \delta_{c,x}^2$ and $\mu_l \partial^2 u / \partial y^2 \sim \mu_l U_b / h^2$. Pressure can be rescaled with the capillary length scale $p \sim \sigma / w$, whereas z can be rescaled by the length of the dynamic meniscus at the bubble front, which is the distance from the bubble tip that it takes for the liquid film to form, and is $\sim w$ [33, 16]. Therefore, Eq. (6) can be approximated as:

$$\text{Ca}_b \left(\frac{1}{\delta_{c,x}^2} + \frac{1}{h^2} \right) \sim \frac{1}{w^2} \quad (7)$$

leading to the following scaling law for the bubble width:

$$\frac{r_{c,x}}{w} \sim 1 - \sqrt{\frac{\text{Ca}_b}{1 - \epsilon^2 \text{Ca}_b}} \quad (8)$$

which explains the reduction of the bubble width with increasing the channel aspect-ratio, observed in Fig. 2. The trend of the bubble width with the aspect-ratio reverses as $\text{Ca}_b \rightarrow 0$ and the bubble dynamics approaches a quasi-static configuration. There exists a threshold value of the capillary number, which decreases with increasing ϵ , below which the cross-sectional distribution of the liquid film rearranges from two semi-circles (or one complete circle for $\epsilon = 1$) to four quarter-circles, connected by thin liquid films. For square channels, this transitional value is of about 0.04 [5, 9]. When Ca_b approaches this value, the rate of increase of the bubble width with decreasing Ca_b subsides, explaining the intersection of the curves for $\epsilon = 1$ and 2 when $\text{Ca}_b \approx 0.01$ in Fig. 2.

Overall, the agreement between the results obtained with the present numerical framework and those of de Lózar et al. [16] is excellent. Deviations appear for increasing values of Ca_b and ϵ due to the finite value of the Reynolds number in our simulations, but the difference in the values of the bubble width between the two studies is always below 3%. Fig. 2 includes also the data for $\epsilon = 1$ published by Magnini and Matar [9], which were obtained using OpenFOAM v. 2.3.1 and the built-in algebraic VOF solver *interFoam*. Although the interface curvature calculation method of *interFoam* is, in principle, less accurate than the parabolic fit presently used, the values of the bubble widths calculated with these two different solvers are almost indistinguishable.

5. Results and discussion

Numerical simulations were performed for a range of capillary and Reynolds numbers of, respectively, $\text{Ca}_1 = 0.005 - 0.5$ and $\text{Re}_1 = 1 - 1000$, and values of the channel aspect-ratio in the range $\epsilon = 1 - 8$. The results are organised in two subsections. Section 5.1 presents the bubble and liquid film dynamics obtained by systematically varying ϵ and Ca_1 , but setting $\text{Re}_1 = 1$ in order to investigate the visco-capillary regime where $\text{We}_1 \ll 1$ and inertial effects are expected to be negligible. Section 5.2 presents the results of simulations run by systematically varying the Reynolds number to investigate the visco-inertial regime ($\text{We}_1 \gg 1$), for two selected values of the capillary number ($\text{Ca}_1 = 0.02$ and 0.1) and one channel aspect-ratio ($\epsilon = 2$).

5.1. Flows with negligible inertia

5.1.1. Liquid film topology

We begin with discussing the topology of the lubricating film in the visco-capillary regime, for the channel aspect-ratios $\epsilon = 2, 4$ and 8, which is illustrated in Figs. 3, 4 and 5. The dynamics for square channels were investigated in detail by Magnini and Matar [31], and thus this section focuses mainly on rectangular channels, $\epsilon > 1$. In Figs. 3, 4 and 5, panels (a) show the contours of the liquid film thickness δ_y , measured as the vertical distance of the liquid-gas interface from the top wall ($y = h$). Panels (b) depict the contours of the liquid film thickness δ_x , measured as the horizontal distance of the interface from the side wall ($x = w$). In (a) and (b), the liquid capillary number is always the same, $\text{Ca}_1 = 0.02$. Panels (c) plot the centreline ($x = 0$) vertical liquid film thickness $\delta_{c,y}$ versus the distance from the bubble nose ($z_N - z$), for different values of Ca_1 . Panels (d) present an analogous plot for the centreline ($y = 0$) horizontal liquid film thickness $\delta_{c,x}$. Panels (e) illustrate the streamwise evolution of the minimum value of the vertical film thickness $\delta_{min,y}$. The final panels (f) illustrate the cross-sectional interface profile, extracted $11R_h$ behind the tip of the bubble nose.

A comparison of the liquid film thickness contours of panels (a) and (b) in Figs. 3, 4 and 5, reveals that for $Ca_1 = 0.02$ the bubble exhibits always a concave surface when observed from the top wall, with the interface curvature changing sign already at very short distance from the bubble nose. This corresponds to the formation of a dimple on the bubble surface, where minimum values of the film thickness (red streaks in panels (a)) are detected. The film thickness decreases monotonically towards the bubble rear along these minimum thickness streaks, owing to the combined effect of liquid film rearrangement by surface tension forces and transversal curvature gradients inducing

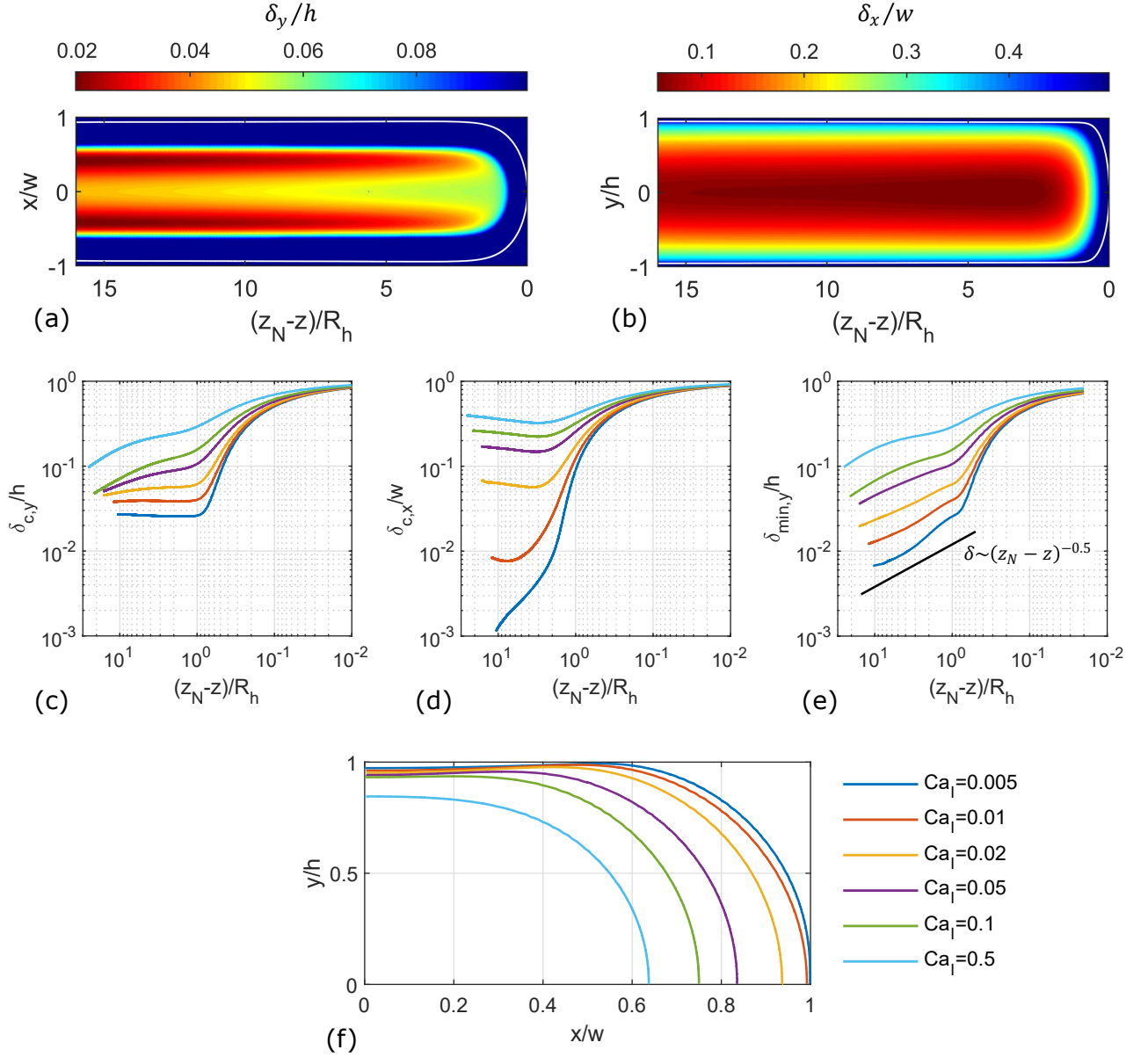


Figure 3: Liquid film morphology for $\epsilon = 2$ ($We_1 \ll 1$). (a,b) Contours of liquid film thicknesses for $Ca_1 = 0.02$, measured as distance from (a) top $y = h$ and (b) side $x = w$ walls; figures not to scale. (c,d,e) Streamwise evolution of the centreline liquid film thickness measured from (c) top and (d) side walls, and (e) minimum liquid film thickness from top wall. (f) Cross-sectional interface profiles extracted $11R_h$ behind the tip of the bubble nose. The legend in (f) applies also to (c,d,e). z_N denotes the bubble nose location. In (a) and (b), the bubble is moving from left to right, and the white line identifies the liquid-gas interface on the (a) $y = 0$ and (b) $x = 0$ planes.

film draining flows [14, 8, 9]. While the minimum film thickness values, relative to the channel height, seem rather constant when varying aspect-ratio ϵ , the relative film thickness at the channel centre increases with increasing ϵ , see panels (a). A comparison of panels (b) suggests that the bubble exhibits always a convex surface when observed from the side wall for $Ca_l = 0.02$, with lateral film thickness values δ_x much larger than δ_y , and increasing as ϵ is increased.

A quantitative analysis of the streamwise evolution of the liquid film when varying capillary number and aspect-ratio is provided in panels (c), (d) and (e) of Figs. 3, 4 and 5. As a general trend, all film thicknesses increase with increasing Ca_l , in line with the traditional lubrication theory [1]. A thin liquid film forms quickly over both shorter (vertical) and longer (horizontal) channel walls, from a distance of approximately $1R_h$ behind the tip of the

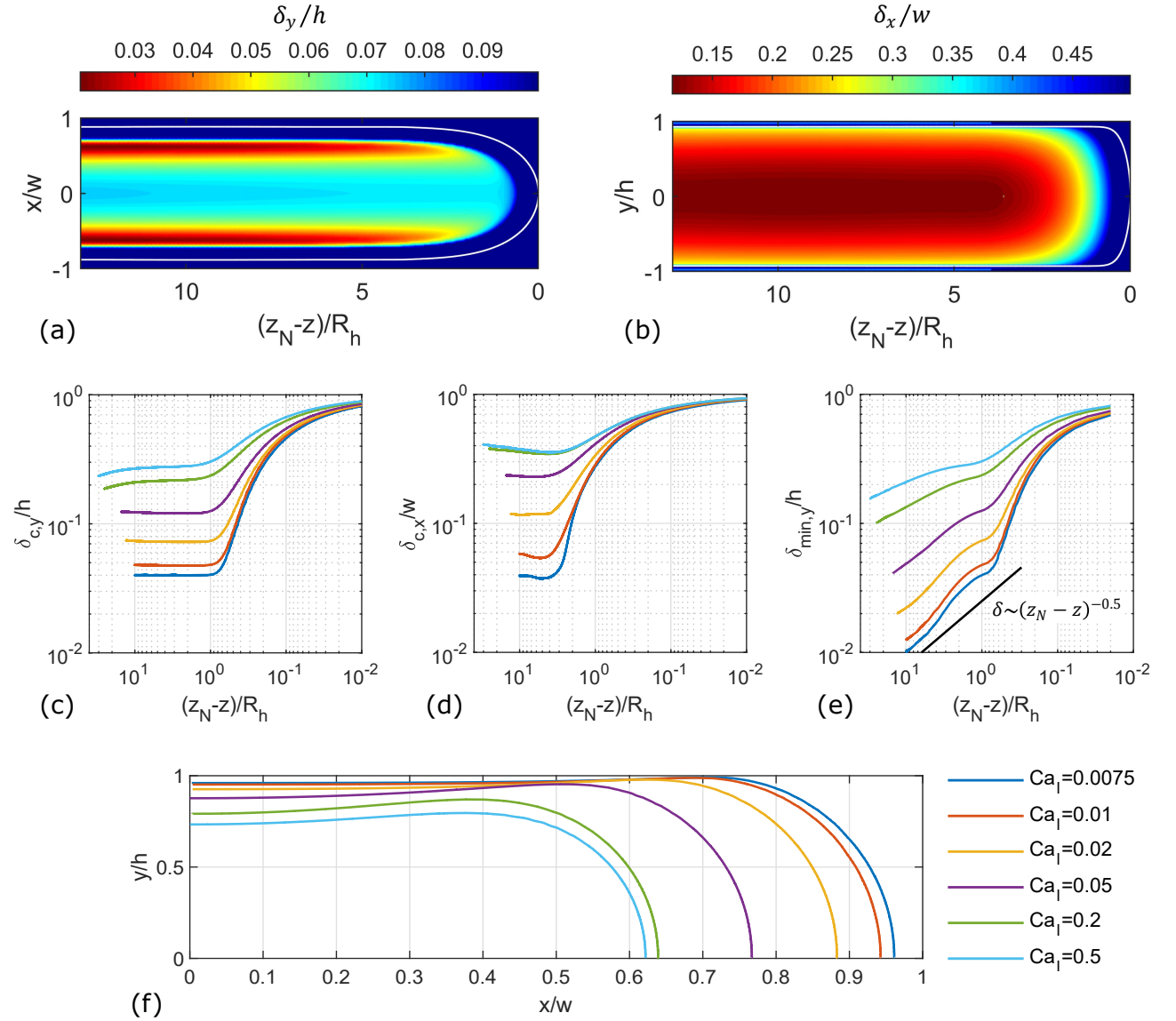


Figure 4: Liquid film morphology for $\epsilon = 4$ ($We_l \ll 1$). (a,b) Contours of liquid film thicknesses for $Ca_l = 0.02$, measured as distance from (a) top $y = h$ and (b) side $x = w$ walls; figures not to scale. (c,d,e) Streamwise evolution of the centreline liquid film thickness measured from (c) top and (d) side walls, and (e) minimum liquid film thickness from top wall. (f) Cross-sectional interface profiles extracted $11R_h$ behind the tip of the bubble nose. The legend in (f) applies also to (c,d,e). z_N denotes the bubble nose location. In (a) and (b), the bubble is moving from left to right, and the white line identifies the liquid-gas interface on the (a) $y = 0$ and (b) $x = 0$ planes.

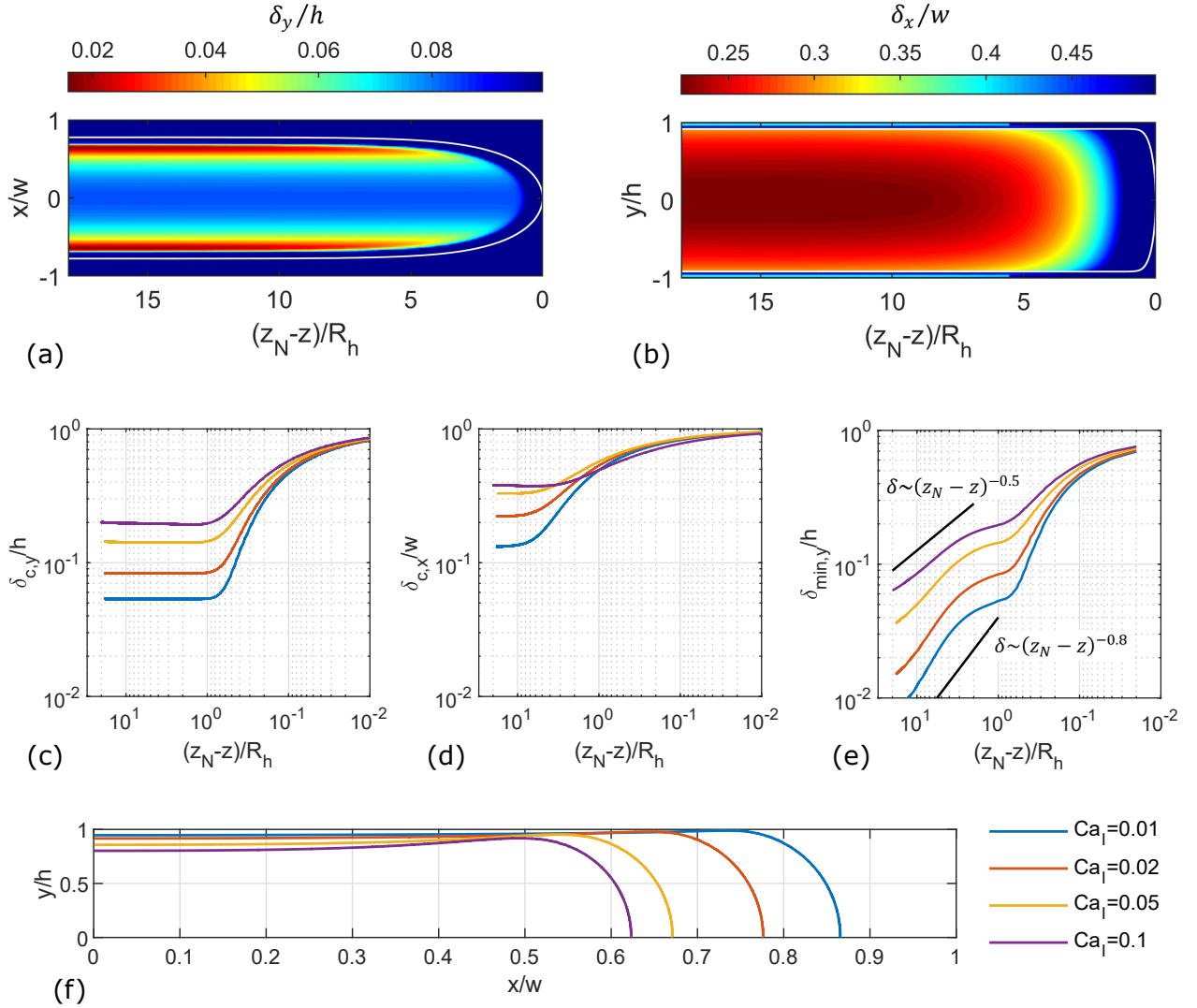


Figure 5: Liquid film morphology for $\epsilon = 8$ ($We_1 \ll 1$). (a,b) Contours of liquid film thicknesses for $Ca_1 = 0.02$, measured as distance from (a) top $y = h$ and (b) side $x = w$ walls; figures not to scale. (c,d,e) Streamwise evolution of the centreline liquid film thickness measured from (c) top and (d) side walls, and (e) minimum liquid film thickness from top wall. (f) Cross-sectional interface profiles extracted $11R_h$ behind the tip of the bubble nose. The legend in (f) applies also to (c,d,e). z_N denotes the bubble nose location. In (a) and (b), the bubble is moving from left to right, and the white line identifies the liquid-gas interface on the (a) $y = 0$ and (b) $x = 0$ planes.

bubble nose. Behind this point, the trends of centreline film thicknesses $\delta_{c,y}$ (panels (c)) and $\delta_{c,x}$ (panels (d)) are strongly dependent on Ca_1 and ϵ . The centreline top film thickness $\delta_{c,y}$ for $\epsilon = 2$, Fig. 3(c), stays rather constant along the bubble body (towards $-z$) for sufficiently small Ca_1 , whereas for $Ca_1 \geq 0.02$ a monotonic decreasing trend towards the bubble rear becomes apparent. The $\epsilon = 4$ channel exhibits a similar behaviour, see Fig. 4(c), although the transition from constant to monotonically decreasing film thickness occurs at higher capillary number, $Ca_1 \geq 0.2$. This decreasing trend is never observed in the largest aspect-ratio channel $\epsilon = 8$, Fig. 5(c), where $\delta_{c,y}$ is constant along the bubble within the range of capillary numbers tested. All these trends are consistent with the asymptotic theory of Wong et al. [14]; Appendix B at the end of this article describes some useful relationships to estimate geometrical features of the liquid film, based on Wong et al. [14]. Wong et al. [14] suggested that behind the bubble front meniscus there exists a first stage of film rearrangement where surface tension rearranges the thin film into a parabolic shape and, at leading-order, the cross-sectional area of the thin film (in the region $-\ell_x \leq x \leq \ell_x$) is conserved, with minimal

streamwise variations of the centreline thickness (Fig. 5 in Wong et al. [14]). This is followed by a second stage, further upstream the bubble body, where transversal drainage flows become important and the film area and thickness reduce monotonically towards the bubble rear. While the latter stage lasts indefinitely, the length of the film rearrangement stage is proportional to $\ell_x^7/(A_0^3 \text{Ca}_b)$ [14], with A_0 being the cross-sectional area of the thin film. Therefore, the length of this first stage decreases as Ca_b increases, and it may become infinitely short at sufficiently large capillary numbers; this corresponds to the situation exemplified in Fig. 3(c), $\epsilon = 2$ and $\text{Ca}_1 \geq 0.05$, where only the second monotonic film thinning stage is present. The length of the rearrangement stage depends also on the channel aspect-ratio via the factor ℓ_x^7/A_0^3 . For increasing ϵ , it follows from Wong et al. [14] theory that both ℓ_x and A_0 are linear functions of ϵ (see Fig. B.1(c) in the Appendix), thus suggesting the scaling $\ell_x^7/A_0^3 \sim \epsilon^4$, i.e. the rearrangement stage grows greatly with increasing the aspect-ratio. This is consistent with the observations in panel (c) of Figs. 3, 4 and 5, and motivates the transition to a monotonically decreasing $\delta_{c,y}$ trend being shifted at progressively larger values of Ca_1 as ϵ is increased, while it does never occur for $\epsilon = 8$. Note that, even for $\epsilon = 8$ or very small capillary numbers, the second film thinning stage would eventually appear at long distance from the bubble nose, much longer than the bubble lengths simulated in this work.

The centreline horizontal film thicknesses for $\epsilon = 2$ and 4, panels (d) in Figs. 3 and 4, exhibit an initially decreasing trend as the front meniscus of the bubble develops towards the rear, followed by a mildly increasing trend once a thin liquid film is formed. The only exception is the case run with $\epsilon = 2$ and $\text{Ca}_1 = 0.005$ (dark blue line in Fig. 3(d)), where the film thins monotonically towards the bubble rear. The trends observed for $\delta_{c,x}$ are related to those discussed previously for the centreline vertical film thickness $\delta_{c,y}$ in panels (c). **Within horizontal channels, the axial flow rate of liquid through the film is very small [10] and, assuming a stagnant film, the overall cross-sectional area occupied by the liquid must be conserved along the bubble. As such, in regions where the top film thickness exhibits an upstream decreasing profile, the side film thickness must increase, and vice versa.** For the largest aspect-ratio channel tested, Fig. 5(d), the centreline horizontal film thicknesses remain approximately constant along the bubble once a thin liquid film is formed, which is consistent with the similar trend exhibited by $\delta_{c,y}$ in Fig. 5(c).

The minimum liquid film thickness $\delta_{min,y}$ measured from the channel top, panels (e) of Figs. 3, 4 and 5, decreases always monotonically towards the bubble rear, as a result of the transversal flows that drive liquid out of the top film. This signifies that liquid film dewetting in elongated bubble flows in noncircular microchannels will always begin from these minimum film thickness regions, as observed in experiments [17, 34]. It is interesting to observe in panels (e) that the streamwise profiles of the minimum film thickness follow quite well the power-law dependence $\delta_{min,y} \sim (z_N - z)^{-\beta}$ for all aspect-ratios tested. Figures 3(e) and 4(e) include the power-law $\delta_{min,y} \sim (z_N - z)^{-0.5}$ as a black line, which matches well the film thickness trends at low capillary numbers. The same dependence was found by Magnini and Matar [9] for bubbles propagating in square channels and by Kreutzer et al. [35] for the capillary-driven drainage of liquid films around long bubbles in noncircular channels. The same exponent for the power-law is found from the film profiles obtained with $\epsilon = 8$ at larger capillary numbers, Fig. 5(e), whereas the slope of the curves increases for decreasing values of Ca_1 , the reason of which can be ascribed to an insufficient length of the bubble to retrieve the asymptotic film thinning trend.

The plots of the cross-sectional profiles of the liquid-gas interface reported in panels (f) of Figs. 3, 4 and 5, indicate that the liquid film over the top wall exhibits always a saddle-like profile, with the generation of a dimple between the wall centre and channel corner, except the $\epsilon = 2$ and $\text{Ca}_1 = 0.5$ case. This is in agreement with the findings of Hazel and Heil [8], who showed that for $\epsilon < 2.04$ it is still possible to attain axisymmetric cross-sectional profiles at sufficiently high Ca_1 . A comparison of the interface profiles for decreasing capillary numbers confirms that the centreline top film thickness $\delta_{c,y}$ decreases at a slower rate than the minimum thickness $\delta_{min,y}$ does, so that dewetting of the film is likely to initiate at the interface dimple.

The results presented in Figs. 3, 4 and 5 were obtained for bubbles of length $L_b > 10R_h$. Since the liquid film dynamics are driven by the bubble nose [30], shorter bubbles are expected to exhibit the same liquid film profiles and thicknesses, provided that $L_b/w > 1$ so that a thin film forms upstream the bubble nose.

5.1.2. Liquid film thickness

In order to compare the values of the liquid film thicknesses obtained with different channel aspect-ratios, Fig. 6 displays centreline horizontal ($\delta_{c,x}$), centreline vertical ($\delta_{c,y}$) and minimum vertical ($\delta_{min,y}$) film thicknesses, measured at a distance of $11R_h$ from the bubble tip, as a function of the bubble capillary number. The data are rescaled by the channel hydraulic radius R_h rather than the height or width, because R_h is maintained constant throughout this study,

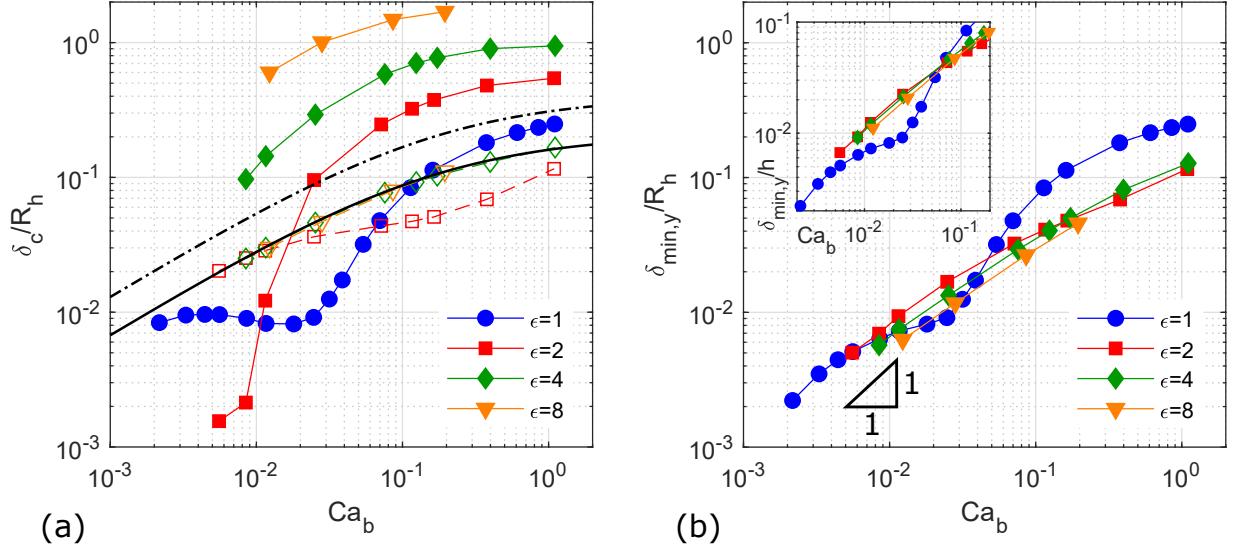


Figure 6: (a) Centreline and (b) minimum film thicknesses measured $11R_b$ behind the tip of the bubble nose, rescaled with the channel hydraulic radius ($We_1 \ll 1$). In (a), the full symbols and solid lines represent the centreline horizontal film thickness, $\delta_{c,x}$, whereas the empty symbols and dashed lines identify the centreline vertical film thickness, $\delta_{c,y}$; the black dash-dot line shows the film thickness prediction for circular tubes obtained using Aussillous and Quéré [2] correlation, Eq. (9); the black solid line identifies the predictions obtained by a modified version of the relationship derived by Wong et al. [14] for the centreline film thickness in noncircular channels, Eq. (10). In (b), the inset shows the minimum thickness data rescaled with the channel height instead of R_b .

whereas h and w vary depending on ϵ as explained in Sec. 3. As such, a comparison of the absolute values of the film thicknesses among the different channel aspect-ratios is possible. The data for $\epsilon = 1$ in Fig. 6 are taken from the previous work of Magnini and Matar [9], which covered a slightly wider range of Ca_1 than the present work, and with more data points. As an additional comparison, Fig. 6(a) includes also a black dash-dot line identifying the predicted values of the film thickness for long bubbles advancing in circular tubes, obtained using Aussillous and Quéré [2] correlation. Bretherton [1] derived theoretically that in the limit of a small capillary number ($Ca_b < 0.005$), the liquid film thickness in circular channels obeys $\delta_{circ}/r = 1.34Ca_b^{2/3}$, where r is the radius of curvature of the bubble nose and was assumed equal to the tube radius R , which is acceptable for small capillary numbers and very thin liquid films. Aussillous and Quéré [2] extended this relationship to $Ca_b \rightarrow 2$ considering that, for a thick film, the radius of curvature of the bubble nose will be smaller than R by an amount proportional to the film thickness, $r = R - c\delta_{circ}$. The constant c was derived empirically by Aussillous and Quéré [2], from a best fit of Taylor's [36] and their own experimental data for very viscous fluids, giving $c = 2.5$ and leading to the following well-known correlation for the liquid film thickness in circular tubes, valid in the limit of negligible inertial effects [2]:

$$\frac{\delta_{circ}}{R} = \frac{1.34Ca_b^{2/3}}{1 + 3.35Ca_b^{2/3}} \quad (9)$$

which yields the prediction identified as a black dash-dot line in Fig. 6(a).

Inspection of Fig. 6(a) reveals that the centreline horizontal thickness $\delta_{c,x}$ is always larger than the vertical one $\delta_{c,y}$, as $w > h$ and therefore the bubble is less confined in the horizontal direction. This trend is reversed for $\epsilon = 2$ and $Ca_b < 0.02$, where the horizontal bubble width $r_{c,x} \rightarrow 1$ and thus $\delta_{c,x}$ drops quickly below $\delta_{c,y}$. The same trend is expected to occur for larger aspect-ratios as well, but at decreasing values of Ca_b for increasing ϵ , and it is never observed in the range of conditions analysed here. While $\delta_{c,x}$ for $\epsilon \geq 2$ is, generally, always above the film thickness that would occur at the same Ca_b in a circular tube, the centreline vertical film thickness $\delta_{c,y}$ is always smaller than the value for a circular channel. The non-monotonic trend of δ_c for $\epsilon = 1$ was investigated in detail by Magnini and Matar [9]. When $Ca_b \geq 0.05$ the bubble cross-section in a square channel is axisymmetric and, as Ca_b is increased,

Fig. 6 reveals that δ_c is larger than $\delta_{c,y}$ in a rectangular duct, but always smaller than $\delta_{c,x}$. As Ca_b is reduced below 0.01, a thin liquid film forms and an interfacial dimple appears, first near the wall centre and then progressively closer to the corner as Ca_b is further reduced. During this process, δ_c first increases slightly as the dimple forms and then reduces monotonically as the dimple shifts sideways. In this range of Ca_b , δ_c for a square channel is always smaller than $\delta_{c,y}$ for a rectangular channel, whereas it is expected to be larger than the horizontal film thickness $\delta_{c,x}$, once that Ca_b is small enough for an interfacial dimple to appear also over the shorter wall, as demonstrated by the data points for $\epsilon = 2$.

It is interesting to observe that, when $\delta_{c,y}$ is rescaled by R_h as done in Fig. 6(a), the data for $\epsilon = 4$ and 8 collapse to a single line throughout the whole range of Ca_b investigated, those for $\epsilon = 2$ reach the same line as $Ca_b \leq 0.01$, and those for $\epsilon = 1$ seem to approach the same curve as $Ca_b \rightarrow 0$. This trend can be explained by extending the asymptotic theory of Wong et al. [14] for $Ca_b \rightarrow 0$, to non-vanishing capillary numbers. Wong et al. [14] predicted that, in the first stage of film rearrangement, the centreline film thickness in a noncircular channel obeys Bretherton's law $\delta_c/r = 1.34Ca_b^{2/3}$, where r is now the radius of the circular arc that the liquid film forms at the channel corner. In quasi-static conditions, r has an analytical expression that, for a rectangular channel cross-section, depends only on ϵ ; this is reported in Appendix B, see Eq. (B.2), and Fig. B.1(a) shows that r is very weakly dependent on ϵ and takes values in the range $r \approx (0.51 - 0.53)R_h$, i.e. the radius of curvature of the static meniscus at the channel corner is about half the hydraulic radius of the channel, irrespective of the aspect-ratio of the cross-section. Taking an average value $r = 0.52R_h$, the scaling law of Wong et al. [14] can be rewritten as $\delta_c/R_h = 0.7Ca_b^{2/3}$, which is independent of the channel aspect-ratio and is valid in the limit of small capillary numbers. This can be extended to larger capillary numbers by applying the same reasoning as Aussillous and Qu  r   [2], thus considering that in the case of a thick liquid film, the radius of curvature of the corner meniscus must reduce to $r - c\delta_c$. Using the same constant $c = 2.5$ as Aussillous and Qu  r   [2], a new correlation for the centreline film thickness in noncircular channels at non-vanishing capillary numbers is finally derived:

$$\frac{\delta_c}{R_h} = \frac{0.7Ca_b^{2/3}}{1 + 3.35Ca_b^{2/3}} \quad (10)$$

This correlation suggests that the centreline film thickness depends only on R_h and is independent of the channel aspect-ratio, in agreement with the trends for $\delta_{c,y}$ emerging from Fig. 6(a), and that this thickness is about half the value that it would take in a circular channel at the same flow conditions. The film thickness prediction by Eq. (10) is indicated as a black solid line in Fig. 6(a) and it fits remarkably well the present numerical data for the vertical film thickness $\delta_{c,y}$. The scaling breaks down above an aspect-ratio-dependent value of Ca_b , e.g. $Ca_b \geq 0.02$ for $\epsilon = 2$, where the film rearrangement stage disappears and thus Eq. (10) does no longer apply.

The values of the minimum film thickness measured from the top wall, $\delta_{min,y}$, are reported as a function of the capillary number in Fig. 6(b). All the data follow the trend $\delta_{min,y} \sim Ca_b^{-1}$ as the capillary number decreases regardless of the channel aspect-ratio, as theoretically derived by Wong et al. [14]. Notably, not only the trends but also the values of the minimum film thicknesses are comparable among the different aspect-ratios as Ca_b is reduced, and the data points for $\epsilon \geq 2$ actually overlap almost perfectly when rescaling $\delta_{min,y}$ with the channel height h , instead of R_h , see the inset in Fig. 6(b). This suggests that the channel height is the controlling parameter for the minimum film thickness $\delta_{min,y}$ in rectangular channels. **The liquid film thicknesses reported in Fig. 6 were extracted at a distance of $11R_h$ from the bubble tip. Bubbles shorter than $11R_h$ would exhibit slightly different film thickness values when this is measured at a shorter distance from the nose, as revealed by analysis presented in Sec. 5.1.1. Figures 3, 4 and 5 suggest that $\delta_{c,x}$ and $\delta_{min,y}$ are more sensitive to the streamwise coordinate, whereas $\delta_{c,y}$ is constant in the first stage of film rearrangement where the data in Fig. 6(a) collapse onto a single curve. As such, Eq. (10) is expected to hold also for shorter bubbles, or centreline film thicknesses measured at shorter distance from the nose.**

The discussion over the liquid film topology concludes with the analysis of Fig. 7, where the transversal distance between the minimum film thickness location and the top wall centre, ℓ_x , is plotted versus the capillary number for the different aspect-ratios tested. Note that, once the dimple is formed near the bubble nose, ℓ_x is constant along the bubble body, as indicated by the red streaks in the film thickness contours of Figs. 3, 4 and 5, panels (a), being parallel to the $x = 0$ plane. For $\epsilon \leq 2$, the dimple first forms near the channel centre ($\ell_x = 0$), whereas for $\epsilon > 2$ the bubble cross-section cannot become axisymmetric and therefore the dimple is always farther from the channel centre. In all cases, the dimple shifts sideways as the capillary number is decreased and ℓ_x approaches an aspect-ratio-dependent

value as $Ca_b \rightarrow 0$, for which a theoretical relationship was provided by Wong et al. [14]:

$$\frac{\ell_x}{w} = 1 - \frac{r}{R_h} \frac{2}{1 + \epsilon} \approx 1 - \frac{1.04}{1 + \epsilon} \quad (11)$$

where we have taken $r \approx 0.52R_h$ to replace for r/R_h . Equation (11) and the data in Fig. 7 may be used to estimate ℓ_x as a function of both ϵ and Ca_b , and thus predict the location where dryout may first occur in a rectangular microchannel (at $x = \ell_x$) or calculate the fraction of the channel wall covered by a thin liquid film (which will be ℓ_x/w), which is of interest in heat transfer applications [37].

5.1.3. Bubble speed and gas area fraction

When an elongated bubble is transported by a liquid flow within a microchannel, the bubble velocity U_b and cross-sectional gas area fraction α (fraction of the channel cross-section occupied by the gas phase) are related by a material balance which, under the assumption of negligible axial flow rate of liquid through the film, states that $U_b/U_l = 1/\alpha$. Figure 8 displays the bubble-to-liquid velocity ratio and gas area fraction as a function of the bubble capillary number for different aspect-ratios, and confirms the opposite trends of U_b/U_l and α vs Ca_b . As $Ca_b \rightarrow 0$, the gas fraction increases and approaches a quasi-static value α_s that depends on ϵ . Wong et al. [14] derived an expression to estimate α_s as a function of ϵ which is reported in Appendix B, see Eq. (B.4), and Fig. B.1(b) shows that $\alpha_s \approx 0.94 - 0.98$ for $\epsilon = 1 - 8$, i.e. the static gas fraction increases only slightly as the channel aspect-ratio is increased. Conversely, $U_b/U_l \rightarrow 1/\alpha_s$ when $Ca_b \rightarrow 0$ and thus the bubble speed data in Fig. 8(a) approach values close to unity regardless of the channel aspect-ratio. As the capillary number is increased, the gas fraction decreases owing to the thicker liquid film and the bubble speed increases. In this regime, the horizontal bubble radius decreases significantly as the aspect-ratio is increased, see Fig. 2, so the gas fraction decreases apparently when ϵ increases, while the bubble travels much faster.

de Lózar et al. [15, 16] observed that there exists a modified capillary number \widehat{Ca}_b that depends on the aspect-ratio, which correlated well their experimental and numerical gas fraction data for all aspect-ratios when $\widehat{Ca}_b > 0.035$. Based on scaling arguments, de Lózar et al. [16] suggested $\widehat{Ca}_b = Ca_b(1 + \epsilon^2/\epsilon_t^2)$, with ϵ_t being a transitional aspect-ratio at which the horizontal and vertical components of the viscous term within the liquid film balance. They proposed $\epsilon_t = 6.4$ according to a best fit of their numerical database. This scaling does not apply at low Ca_b , where the bubble dynamics approaches the quasi-static behaviour and $\alpha \rightarrow \alpha_s$, with α_s depending on ϵ as derived by Wong et al. [14]

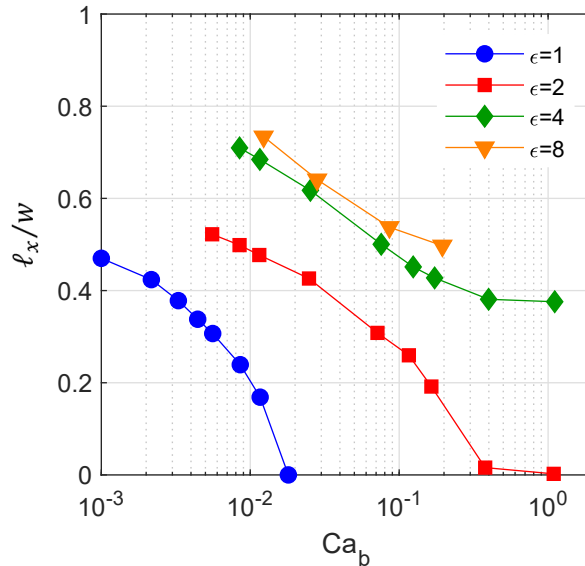


Figure 7: Transversal distance ℓ_x between minimum film thickness location and top wall centre $x = 0$ ($We_l \ll 1$); see schematic in Fig. 1.

and reported in Appendix B. To obtain a general correlation to predict both α and U_b/U_l as a function of Ca_b and ϵ at all regimes, we first replot the gas fraction as α/α_s , and the bubble-to-liquid speed ratio as $(U_b/U_l)\alpha_s$, see the insets in Fig. 8, so that they both approach unity as $Ca_b \rightarrow 0$. The data are presented as a function of a modified capillary number, $\widehat{Ca}_b = Ca_b(1 + \epsilon^2/\epsilon_l^2)$, with ϵ_l obtained by a best fit to our database. We assume the following functional relationship:

$$\frac{\alpha}{\alpha_s} = f(\widehat{Ca}_b) = 1 - (1 - \alpha_\infty) \exp(a_1 \widehat{Ca}_b^{a_2}) \quad (12)$$

where α_∞ is the asymptotic gas fraction for $Ca_b \rightarrow \infty$ and is taken from the correlation of Aussillous and Quéré [2] for flow in circular channels, $\alpha_\infty = 0.37$. Since the gas fraction must approach the static value as the quasi-static regime is recovered ($Ca_b \rightarrow 0$), a_1 and a_2 in Eq. (12) must be negative. A least-squares fit is performed to find ϵ_l , a_1 and a_2 based on our database. This yields $\epsilon_l = 5.5$, $a_1 = -0.24$ and $a_2 = -0.5$. The prediction of α/α_s obtained with Eq. (12) can be used also to estimate the bubble-to-liquid velocity ratio, as $(U_b/U_l)\alpha_s = \alpha_s/\alpha$, with α_s then calculated according to Eq. (B.4). It can be seen in Fig. 8 that the scaling proposed is effective in collapsing all the data for different aspect-ratios onto a single curve throughout the entire range of Ca_b investigated. Note that Eq. (12) can be used to predict the gas fraction (or bubble speed) even if the bubble capillary number is not known, assuming that Ca_l is available. It is sufficient to start with Ca_l in place of Ca_b in Eq. (12) to extract a first guess of α , then using the material balance $U_b/U_l = 1/\alpha$ to calculate a first guess for Ca_b , and iterate between Eq. (12) and the material balance until converged values of α and Ca_b are achieved.

5.2. Flows with inertia

Inertial forces generally impact the bubble dynamics by thinning the liquid film in an intermediate range of Reynolds numbers, $Re = 100 - 500$, whereas as Re is further increased the film thickens monotonically [38, 3, 9]. The bubble nose elongates for increasing Reynolds numbers and the thin liquid film forms at increasing distance from the bubble nose. Furthermore, inertia is responsible for the appearance and growth of undulations on the liquid-gas interface, in the proximity of the bubble rear meniscus, as the Weber number of the flow exceeds a threshold value of about 0.1 [4, 39, 40].

In this section, the impact of inertial forces on the bubble and liquid film dynamics is investigated for a rectangular channel of aspect-ratio $\epsilon = 2$. The streamwise evolution of the liquid film along the bubble and cross-sectional profiles

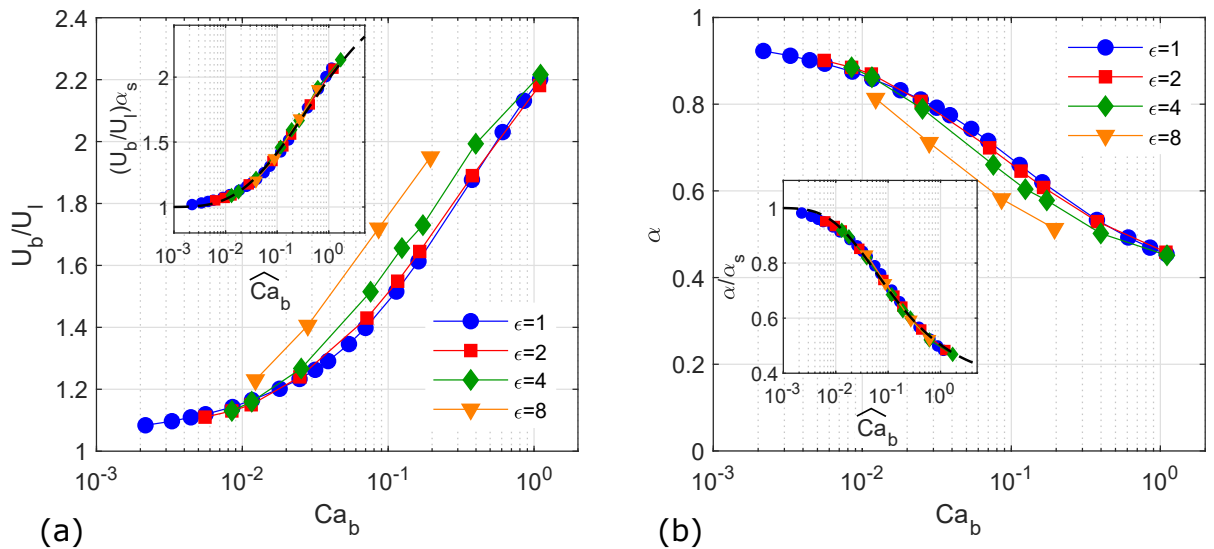


Figure 8: (a) Bubble-to-liquid speed ratio and (b) cross-sectional gas fraction ($We_l \ll 1$). The insets show the (a) bubble velocity data rescaled by the inverse of the static void fraction $1/\alpha_s$ and the (b) void fraction data rescaled by the static void fraction α_s , both plotted versus the rescaled capillary number $\widehat{Ca}_b = Ca_b(1 + \epsilon^2/\epsilon_l^2)$, with $\epsilon_l = 5.5$; the black dashed lines show the prediction obtained using Eq. (12).

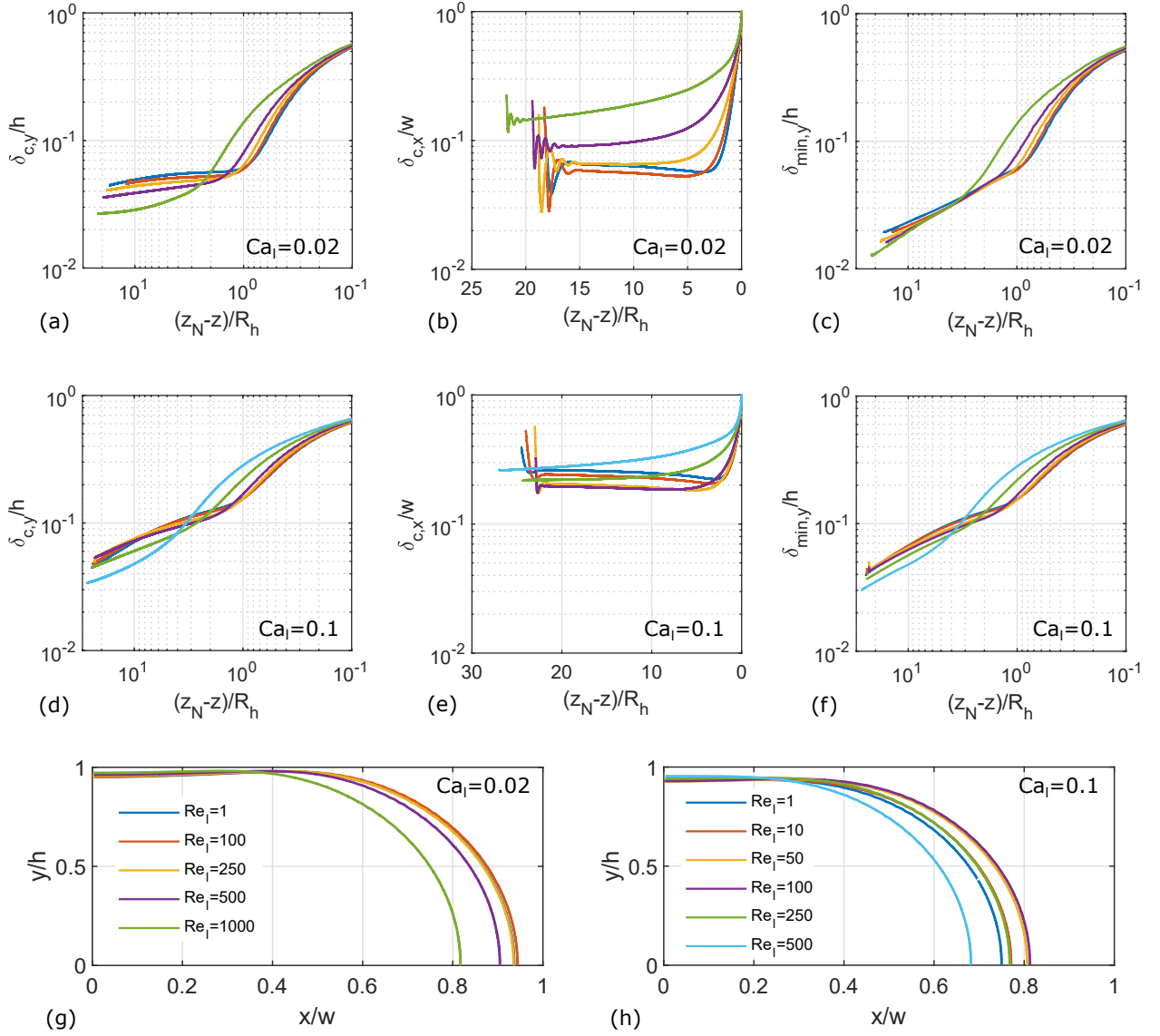


Figure 9: Effect of the Reynolds number, for $\epsilon = 2$, on the streamwise evolution of the (a,d) centreline vertical, (b,e) centreline horizontal and (c,f) minimum liquid film thickness, for (a,b,c) $Ca_1 = 0.02$ and (d,e,f) $Ca_1 = 0.1$. (g,f) Cross-sectional interface profiles extracted $11R_h$ behind the tip of the bubble nose. The legend in (g) applies also to (a,b,c) and that in (h) applies also to (d,e,f).

of the liquid-gas interface are displayed in Fig. 9, for $Ca_1 = 0.02$ and 0.1 and a range of Reynolds numbers. As the Reynolds number is increased, Fig. 9(a,d) confirm that the distance from the bubble nose at which the liquid film forms increases, from about $1R_h$ as long as $We_1 = Ca_1 Re_1 \leq 10$ to $5R_h - 10R_h$ at the largest Reynolds numbers tested. Once the film is formed, the vertical film thickness $\delta_{c,y}$ decreases as Re_1 is increased for $Ca_1 = 0.02$, whereas this dependence is not monotonic for $Ca_1 = 0.1$ and it depends greatly on the distance from the bubble nose. The profiles of the horizontal film thickness $\delta_{c,x}$, depicted in Fig. 9(b,e), exhibit a marked change when the Weber number of the flow transitions above 10, with $\delta_{c,x}$ first increasing and then decreasing towards the upstream direction when Re_1 is increased. As already discussed for Figs. 3, 4 and 5, the streamwise trends of $\delta_{c,x}$ oppose those for $\delta_{c,y}$ because the cross-sectional area occupied by the liquid must be conserved along the bubble. It is interesting to observe that interfacial undulations appear near the bubble rear along the thicker lateral film, see the oscillations in the plot of $\delta_{c,x}$

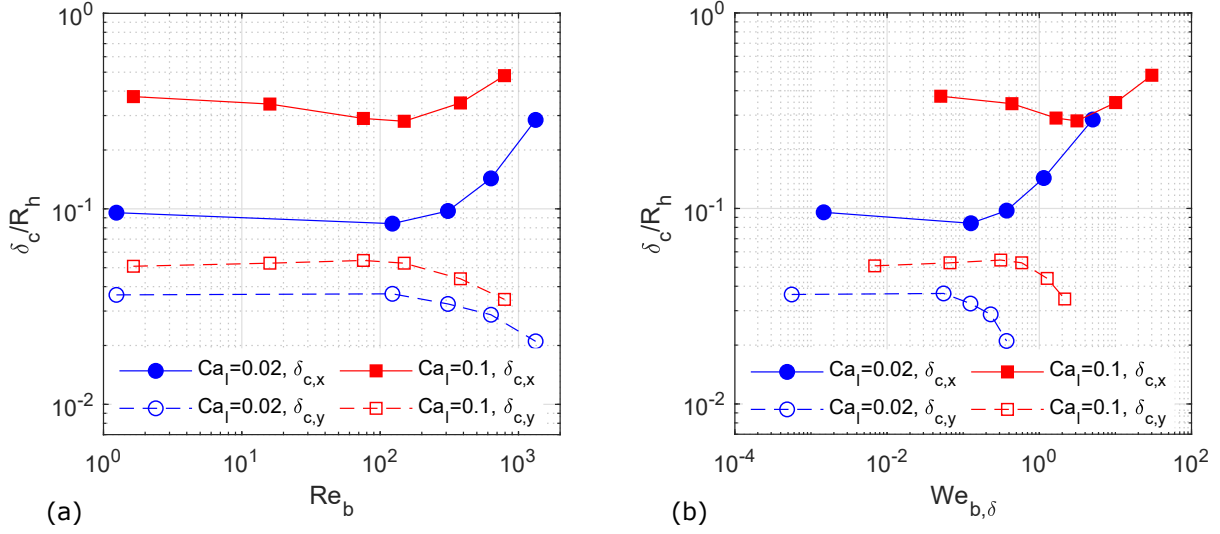


Figure 10: Effect of the Reynolds number, for $\epsilon = 2$, on the centreline horizontal and vertical film thicknesses, measured $11R_h$ behind the tip of the bubble nose and rescaled with the channel hydraulic radius. In (a) the data are displayed versus the bubble Reynolds number, $Re_b = 2\rho_l U_b R_h / \mu_l$, whereas in (b) data are replotted as a function of the film Weber number, $We_{b,\delta} = \rho_l U_b^2 \delta_c / \sigma$, where δ_c is either $\delta_{c,x}$ or $\delta_{c,y}$.

for $Ca_1 = 0.02$. These possess the same geometric features identified by Magnini et al. [4] on long bubbles translating in circular channels. Only one undulation is present when $Re_1 = 1$ and inertial effects are negligible, but multiple crests become apparent as $Re_1 \geq 100$. Inertia-driven undulations are absent on the top of the bubble, where the profiles of $\delta_{c,y}$ appear smooth, because the liquid film is much thinner (inertial effects scale with the local film thickness), and do not appear for $Ca_1 = 0.1$ despite the larger Weber numbers, as the damping effect of viscous forces prevail [4, 39]. The minimum film thickness $\delta_{min,y}$, reported in Fig. 9(c) and (f), exhibits monotonic decreasing trends towards the bubble rear for all the conditions investigated. Corresponding profiles of the bubble interface on the cross-section are shown in Fig. 9(g) and (h), and reveal that as the Reynolds number is increased the bubble cross-section shrinks and the change in concavity of the top film becomes less apparent. For $Ca_1 = 0.1$ and $Re_1 = 500$, cyan profile in Fig. 9(h), no dimple has yet formed in the displayed profile, which is extracted $11R_h$ behind the tip of the bubble nose, because it takes about $20R_h$ from the bubble front tip for the curvature of the top film to change sign and the dimple to appear.

The centreline vertical and horizontal film thickness data in the presence of inertial effects, measured $11R_h$ behind the tip of the bubble nose, are compiled in Fig. 10. Figure 10(a) confirms that the horizontal film thickness $\delta_{c,x}$ exhibits first a descending and then a monotonic ascending trend as Re_1 increases, in agreement with the observations taken in square [9] and circular channels [38, 3]. The film measured along the vertical direction, $\delta_{c,y}$, is significantly thinner and follows a monotonic descending trend throughout the range of Re_1 tested, so that when $Re_1 > 100$, the thicker lateral film thickens further while the thinner top film gets even thinner. Since the Weber number and the local film thickness are more suitable indicators of the importance of inertial forces on the film dynamics, Fig. 10(b) replots the data as a function of the film Weber number, defined as $We_{b,\delta} = \rho_l U_b^2 \delta_c / \sigma$. This rescaling has the effect of shifting the $\delta_{c,y}$ data to the left, as they are characterised by a smaller $We_{b,\delta}$ than $\delta_{c,x}$. It can be seen that, for each Ca_1 tested, the descending trends for both $\delta_{c,x}$ and $\delta_{c,y}$ occur approximately in the same range of $We_{b,\delta}$, thus suggesting that inertial effects appear at larger Re_1 on the thinner film on top, being this one order of magnitude thinner than the film at the side.

6. Conclusions

The topology of the liquid film formed around long gas bubbles advancing in noncircular channels has been investigated systematically, for a range of cross-sectional aspect-ratios $\epsilon = 1 - 8$, liquid capillary numbers $Ca_1 = 0.005 - 0.5$ and Reynolds numbers $Re_1 = 1 - 1000$, thus covering both the visco-capillary and visco-inertial regimes.

The analysis is based on the results of direct numerical simulations conducted utilising a geometric Volume-Of-Fluid method as implemented in the TwoPhaseFlow library for OpenFOAM recently released by Scheufler and Roenby [19]. The interface curvature, which enters the calculation of the surface tension force and is crucial for the accuracy of the numerical method when applied to low capillary number flows, is estimated based on a geometric parabolic reconstruction method. The main conclusions of this work, applicable to the range of conditions studied, are as follows:

- The bubble cross-sections exhibit circular arcs at the sides, nearby the shorter wall, and a flatter interface with a wide saddle-shaped liquid film along the longer wall.
- The different lengths of the channel sides ($\epsilon > 1$) induce different dynamics of the liquid film draining flows in the two sides. As a consequence, the streamwise evolution of the liquid film along the bubble shows distinctive features depending on the channel aspect-ratio, capillary and Reynolds numbers, and a region of uniform film thickness along the bubble is never observed.
- The thickness of the film covering the longer channel wall, measured along the centreline, is constant along the bubble at small Ca , whereas it decreases monotonically towards the bubble rear above a threshold value for Ca , which increases as the aspect-ratio increases. This agrees with the asymptotic theory of Wong et al. [14] for $Ca \rightarrow 0$, which suggested the existence of a region of constant film area within a distance of order ϵ^4/Ca from the bubble front meniscus, followed by a monotonic film thinning stage closer to the bubble rear.
- The film thickness measured along the centreline of the longer wall obeys the scaling law $\delta_{c,y}/R_h \sim Ca^{2/3}/(1 + Ca^{2/3})$ regardless of the channel aspect-ratio (for $\epsilon > 1$), and takes values that are about half those characteristic of flows in a circular channel at the same conditions.
- The cross-sectional gas fraction decreases when the aspect-ratio increases owing to the thick liquid film left over the shorter wall. However, the gas fraction α trends vs Ca are all similar and we propose an empirical correlation to predict α as a function of Ca and ϵ , that matches well the present data from $Ca \rightarrow 0$ to $Ca \approx 1$.
- Inertial effects on the liquid film topology are more apparent on the side of the channel where a thicker film is present; this exhibits first a thinning and then a thickening trend as Re is increased. The thinner film deposited along the longer wall shows only the initial descending trend.

Acknowledgements

This work is supported by the UK Engineering & Physical Sciences Research Council (EPSRC), through the BONSAI (EP/T033398/1) grant. We acknowledge the use of Athena at HPC Midlands+, which was funded by the EPSRC grant EP/P020232/1, as part of the HPC Midlands+ consortium. The authors wish to thank Henning Scheufler (German Aerospace Center, DLR, Bremen) for sharing their self-developed OpenFOAM libraries before publication.

Appendix A. Evaluation of spurious velocity

In order to evaluate the performance of the different surface tension models implemented in the TwoPhaseFlow library [19], we have performed a traditional two-dimensional static bubble test case, which enables to quantify the magnitude of the spurious currents generated by inaccuracies in the surface tension calculation. The configuration simulated is taken from Gamet et al. [41] and the simulation setup was downloaded from the link that they provide at the end of the Conclusion section of their article; we refer to their article for the details of the solution algorithm options. A circular bubble of diameter $D = 0.8$ m is placed within a liquid-filled domain. Only a quarter of the geometry is simulated in a domain of size 1×1 m, and the bubble is centred at one corner of the domain. The fluid properties are: $\rho_l = \rho_g = 1$ kg/m³, $\sigma = 1$ N/m. The viscosities of liquid and gas are the same and the value chosen to match a Laplace number $La = \rho D \sigma / \mu^2 = 120$. Symmetry boundary conditions are applied to all boundaries. The fluid is initially at rest. A uniform structured mesh with 32×32 square cells is utilised to discretise the domain, so that the bubble is meshed with about 25 cells per diameter. The simulation is run with a constant time step of 10^{-3} s

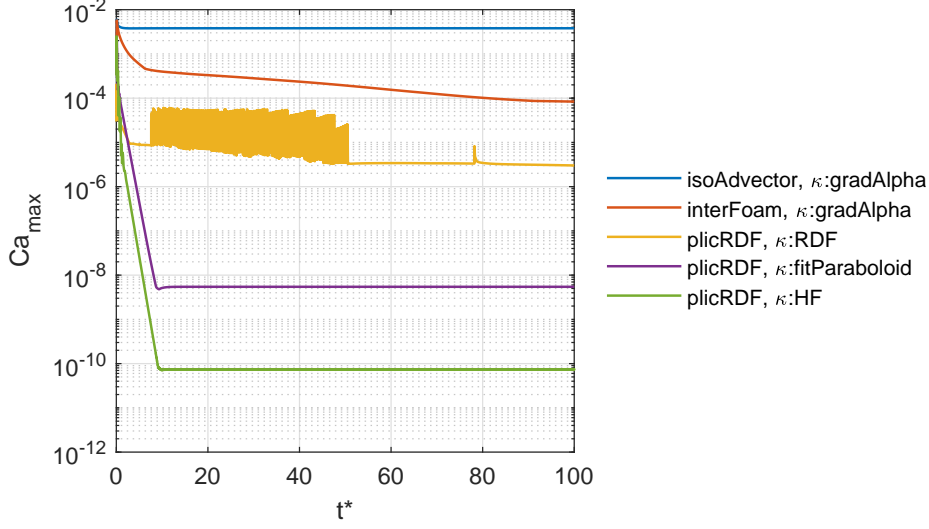


Figure A.1: Maximum capillary number, $Ca_{\max} = \mu U_{\max}/\sigma$, versus nondimensional time, $t^* = t/t_{cap}$ with $t_{cap} = \sqrt{\rho D^3/\sigma}$, for the static bubble test case performed with different advection and curvature calculation methods available in the library TwoPhaseFlow [19]: gradAlpha stands for $\kappa = \nabla \cdot (\nabla c/|\nabla c|)$, RDF stands for Reconstructed Distance Function, fitParaboloid identifies the parabolic fit adopted in this work, whereas HF stands for Height Function method.

for an overall sampling time of $t = 71.5$ s, which is much larger than the characteristic time of the spurious velocity generated and thus enables a robust statistical analysis [42].

The temporal evolution of the maximum value of the spurious velocity generated within the domain is presented in Fig. A.1 for the different algorithms tested. The reference case is OpenFOAM’s built-in isoAdvector (geometric VOF) solver, with the interface curvature κ within the surface tension force term calculated based on the gradients of the volume fraction. This yields the largest spurious currents, with magnitude little below 10^{-2} in nondimensional units. InterFoam performs slightly better, owing to the algebraic VOF that allows a smoother interface, thus making the gradients of the volume fraction better representative of the interface geometry. The use of the plic-RDF option in isoAdvector for the interface advection alone does not impact the magnitude of the spurious velocities, but the use of the reconstructed distance function to evaluate κ yields a significant reduction of Ca_{\max} compared to the reference case. The best performances are achieved by the parabolic reconstruction and the Height Function method. Since the latter is limited to square/cubic mesh cells only, the parabolic reconstruction has been chosen to perform the study presented in this article. **The results of additional benchmark tests for the different surface tension algorithms available in the TwoPhaseFlow library are included in the article of Scheufler and Roenby [19].**

Appendix B. Liquid film features from the asymptotic solution of Wong et al. [14]

We report here the evaluation of selected geometrical features of the liquid film surrounding long bubbles advancing in rectangular channels, evaluated based on the asymptotic solution of Wong et al. [14] for $Ca \rightarrow 0$. Figure B.1(a) displays the radius of curvature of the circular arc formed by the static meniscus at the corner of the channel cross-section. This is calculated as [14]:

$$\frac{r}{h} = \frac{2\epsilon}{\epsilon + 1 + [(\epsilon - 1)^2 + \pi\epsilon]^{1/2}} \quad (\text{B.1})$$

where h is the channel half-height and, since $h/R_h = (1 + \epsilon)/(2\epsilon)$:

$$\frac{r}{R_h} = \frac{\epsilon + 1}{\epsilon + 1 + [(\epsilon - 1)^2 + \pi\epsilon]^{1/2}} \quad (\text{B.2})$$

which is plotted in Fig. B.1(a) as a function of the channel aspect-ratio ϵ .

The static cross-sectional gas fraction is approximated by taking the area of a quarter of the cross-section and subtracting the area of the circular liquid lobe left at the corner (see insets in Fig. B.1(a)):

$$\alpha_s = \frac{hw - r^2(1 - \pi/4)}{hw} \quad (\text{B.3})$$

where w is the channel half-width and, rearranging:

$$\alpha_s = 1 - \frac{1 - \pi/4}{\epsilon} \left(\frac{r}{h}\right)^2 \quad (\text{B.4})$$

where r/h can be calculated via Eq. (B.1). The static gas fraction obtained using Eq. (B.4) is plotted in Fig. B.1(b).

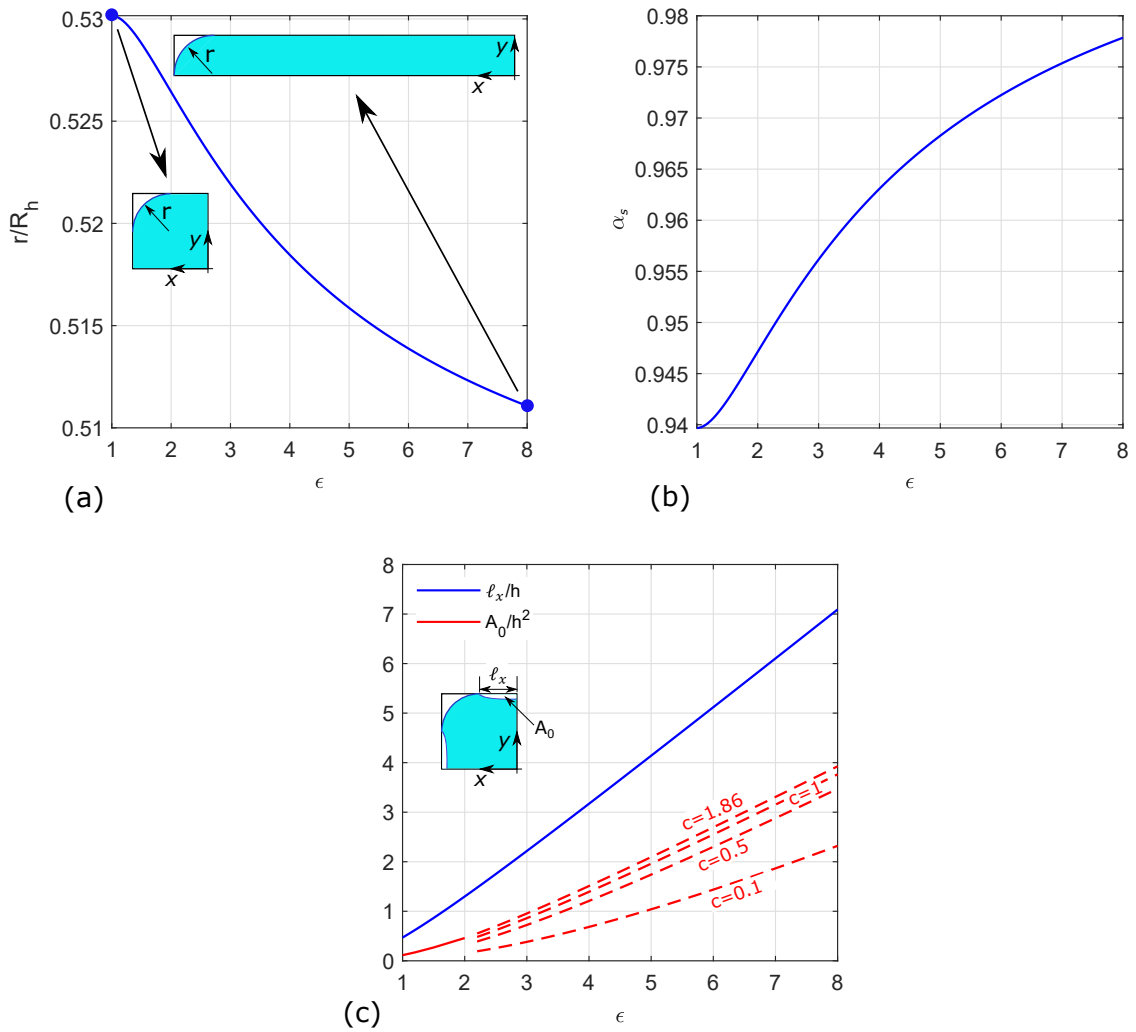


Figure B.1: Results from the theory of Wong et al. [14]: (a) radius of curvature r of the circular arc formed by the meniscus at the corner of the channel cross-section, Eq. (B.2); (b) cross-sectional static gas fraction α_s , Eq. (B.4); (c) transversal distance l_x between minimum film thickness location and channel centre, Eq. (11), and cross-sectional half-area of the thin film A_0 , Eq. (B.5). The insets in (a) depict the bubble and liquid film distribution on the channel cross-section for $\epsilon = 1$ and 8. The inset in (c) identifies the thin film region of half-area A_0 . The red solid line is obtained using Eq. (B.6) with aspect-ratio-dependent values of c from Wong et al. [14], whereas the dashed lines are obtained using arbitrary constant values of c .

The transversal distance ℓ_x between minimum film thickness location and channel centre along the width is calculated as indicated in Eq. (11) and the result is displayed in Fig. B.1(c). The figure reports also the plot of the cross-sectional half-area of the thin film in the first stage of film rearrangement which, according to Wong et al. [14], can be obtained by integrating the film profile:

$$\frac{A_0}{h^2} = \frac{1}{(3Ca_b)^{2/3}} \int_0^{\ell_x} \delta_0(x) dx \quad (\text{B.5})$$

with the film profile $\delta_0(x)$ expressed as:

$$\frac{\delta_0}{h} = 1.34 \left(\frac{r}{h}\right) Ca_b^{2/3} \left[1 + \left(\frac{\pi}{2\ell_x c}\right)^2 \tan^2\left(\frac{\pi x}{2\ell_x}\right) \right]^{-1/3} \quad (\text{B.6})$$

with c being a constant that identifies the shape of the apparent contact line at the bubble front. This constant depends on ϵ and does not have an analytical expression. Wong et al. [14] calculated it by fitting their numerical results and provided values only for $1 \leq \epsilon \leq 2$. The resulting trend of A_0 within this range is displayed as a red solid line in Fig. B.1(c). To extrapolate A_0 to larger aspect-ratios, we used Eqs. (B.5) and (B.6) with four selected values of c : $c = 1.86$, which is the actual value corresponding to $\epsilon = 2$, and three lower values, because c decreases with increasing ϵ . The four extrapolated trends are plotted in Fig. B.1(c) with red dashed lines and indicate that, regardless of the value of c , the film area is approximately a linear function of ϵ as $\epsilon > 1$. Since Fig. B.1(c) shows that $\ell_x \sim \epsilon$ as well, this justifies the assumption made in Sec. 5.1.1 that the length of the first stage of film rearrangement $\ell_x^*/(A_0^3 Ca_b)$ can be well approximated as ϵ^4/Ca_b .

References

- [1] F. P. Bretherton, The motion of long bubbles in tubes, *J. Fluid Mech.* 10 (1961) 166–188.
- [2] P. Aussillous, D. Quéré, Quick deposition of a fluid on the wall of a tube, *Phys. Fluids* 12 (2000) 2367–2371.
- [3] Y. Han, N. Shikazono, Measurement of liquid film thickness in micro square channel, *Int. J. Multiph. Flow* 35 (2009) 896–903.
- [4] M. Magnini, A. Ferrari, J. R. Thome, H. A. Stone, Undulations on the surface of elongated bubbles in confined gas-liquid flows, *Phys. Rev. Fluids* 2 (2017) 084001.
- [5] J. Ratulowski, H.-C. Chang, Transport of gas bubbles in capillaries, *Phys. Fluids A* 1 (1989) 1642–1655.
- [6] W. B. Kolb, R. L. Cerro, Coating the inside of a capillary of square cross-section, *Chem. Eng. Sci.* 46 (1991) 2181–2195.
- [7] W. B. Kolb, R. L. Cerro, The motion of long bubbles in tubes of square cross-section, *Phys. Fluids A* 5 (1993) 1549–1557.
- [8] A. L. Hazel, M. Heil, The steady propagation of a semi-infinite bubble into a tube of elliptical or rectangular cross-section, *J. Fluid Mech.* 470 (2002) 91–114.
- [9] M. Magnini, O. K. Matar, Morphology of long gas bubbles propagating in square capillaries, *Int. J. Multiph. Flow* 129 (2020) 103353.
- [10] M. T. Kreutzer, F. Kapteijn, J. A. Moulijn, J. J. Heiszwolf, Multiphase monolith reactors: Chemical reaction engineering of segmented flow in microchannels, *Chem. Eng. Sci.* 60 (2005) 5895–5916.
- [11] H. Moran, M. Magnini, C. N. Markides, O. K. Matar, Inertial and buoyancy effects on the flow of elongated bubbles in horizontal channels, *Int. J. Multiph. Flow* 135 (2021) 103468.
- [12] Y. E. Yu, M. Magnini, L. Zhu, S. Shim, H. A. Stone, Non-unique bubble dynamics in a vertical capillary with an external flow, *J. Fluid Mech.* 911 (2021) A34.
- [13] V. S. Ajaev, G. M. Homsy, Modeling shapes and dynamics of confined bubbles, *Annu. Rev. Fluid Mech.* 38 (2006) 277–307.
- [14] H. Wong, C. J. Radke, S. Morris, The motion of long bubbles in polygonal capillaries. Part 1. Thin films, *J. Fluid Mech.* 292 (1995) 71–94.
- [15] A. de Lózar, A. L. Hazel, M. Heil, Scaling properties of coating flows in rectangular channels, *Phys. Rev. Lett.* 99 (2007) 234501.
- [16] A. de Lózar, A. Juel, A. L. Hazel, The steady propagation of an air finger into a rectangular tube, *J. Fluid Mech.* 614 (2008) 173–195.
- [17] S. Khodaparast, M. K. Kim, J. Silpe, H. A. Stone, Bubble-driven detachment of bacteria from confined micro-geometries, *Environ. Sci. Technol.* 51 (2017) 1340–1347.
- [18] C. W. Hirt, B. D. Nichols, Volume of fluid (VOF) method for the dynamics of free boundaries, *J. Comput. Phys.* 39 (1981) 201–225.
- [19] H. Scheffler, J. Roenby, TwoPhaseFlow: An OpenFOAM based framework for development of two phase flow solvers, *arXiv* (2021) <https://arxiv.org/abs/2103.00870>.
- [20] J. Roenby, H. Bredmose, H. Jasak, A computational method for sharp interface advection, *R. Soc. Open Sci.* 3 (2016) 160405.
- [21] H. Scheffler, J. Roenby, Accurate and efficient surface reconstruction from volume fraction data on general meshes, *J. Comput. Phys.* 383 (2019) 1–23.
- [22] D. L. Youngs, Time-dependent multi-material flow with large fluid distortion, in: K. W. Morton, M. J. Baines (Eds.), *Numerical Methods for Fluid Dynamics*, Academic Press, 1982, pp. 273–285.
- [23] H. G. Weller, A new approach to VOF-based interface capturing methods for incompressible and compressible flows, *OpenCFD Ltd. Report TR/HGW/04* (2008).

- [24] J. U. Brackbill, D. B. Kothe, C. Zemach, A continuum method for modeling surface tension, *J. Comput. Phys.* 100 (1992) 335–354.
- [25] T. Abadie, J. Aubin, D. Legendre, On the combined effects of surface tension force calculation and interface advection on spurious currents within Volume of Fluid and Level Set frameworks, *J. Comput. Phys.* 297 (2015) 611–636.
- [26] B. van Leer, Towards the ultimate conservative difference scheme. V. A second-order sequel to Godunov’s method, *J. Comput. Phys.* 32 (1979) 101–136.
- [27] R. I. Issa, Solution of the implicitly discretized fluid flow equations by operator-splitting, *J. Comput. Phys.* 62 (1985) 40–65.
- [28] A. Satter, G. M. Iqbal, *Reservoir Engineering*, Elsevier, Amsterdam, The Netherlands, 2016.
- [29] S. Szczukiewicz, M. Magnini, J. R. Thome, Proposed models, ongoing experiments, and latest numerical simulations of microchannel two-phase flow boiling, *Int. J. Multiph. Flow* 59 (2014) 84–101.
- [30] E. Yu, L. Zhu, S. Shim, J. Eggers, H. A. Stone, Time-dependent motion of a confined bubble in a tube: transition between two steady states, *J. Fluid Mech.* 857 (2018) R4.
- [31] M. Magnini, O. K. Matar, Numerical study of the impact of the channel shape on microchannel boiling heat transfer, *Int. J. Heat Mass Transf.* 150 (2020) 119322.
- [32] S. Popinet, Numerical models of surface tension, *Annu. Rev. Fluid Mech.* 50 (2018) 49–75.
- [33] P. Tabeling, G. Zocchi, A. Libchaber, An experimental study of the Saffman-Taylor instability, *J. Fluid Mech.* 177 (1987) 67–82.
- [34] S. Khodaparast, O. Atasi, A. Deblais, B. Scheid, H. A. Stone, Dewetting of thin liquid films surrounding long bubbles in microchannels, *Langmuir* 34 (2018) 1363–1370.
- [35] M. T. Kreutzer, M. S. Shah, P. Parthiban, S. A. Khan, Evolution of nonconformal Landau-Levich-Bretherton films of partially wetting liquids, *Phys. Rev. Fluids* 3 (2018) 014203.
- [36] G. I. Taylor, Deposition of a viscous fluid on the wall of a tube, *J. Fluid Mech.* 10 (1960) 161–165.
- [37] A. H. Al-Zaidi, M. M. Mahmoud, T. G. Karayiannis, Effect of aspect ratio on flow boiling characteristics in microchannels, *Int. J. Heat Mass Transf.* 164 (2021) 120587.
- [38] M. T. Kreutzer, F. Kapteijn, J. A. Moulijn, C. R. Kleijn, J. J. Heiszwolf, Inertial and interfacial effects on pressure drop of Taylor flow in capillaries, *AIChE J.* 51 (2005) 2428–2440.
- [39] M. Magnini, A. Beisel, A. Ferrari, J. R. Thome, Pore-scale analysis of the minimum liquid film thickness around elongated bubbles in confined gas-liquid flows, *Adv. Water Resour.* 109 (2017) 84–93.
- [40] E. L. Sharaborin, O. A. Rogozin, A. R. Kasimov, Computational study of the dynamics of the Taylor bubble, *Fluids* 6 (2021) 389.
- [41] L. Gamet, M. Scala, J. Roenby, H. Scheufler, J.-L. Pierson, Validation of volume-of-fluid OpenFOAM isoAdvector solvers using single bubble benchmarks, *Comput. Fluids* 213 (2020) 104722.
- [42] M. Magnini, B. Pulvirenti, J. R. Thome, Characterization of the velocity fields generated by flow initialization in the CFD simulation of multiphase flows, *Appl. Math. Model* 40 (2016) 6811–6830.